1-1-1980

Ternary partition coefficients in Fe-Ni-X alloys--implications on the solidification of iron meteorites.

Chandrasekhar Narayan

TERNARY PARTITION COEFFICIENTS IN Fe-Ni-X ALLOYS--IMPLICATIONS ON THE SOLIDIFICATION OF IRON METEORITES

by

Chandrasekhar Narayan

A Thesis

Presented to the Graduate Committee

of Lehigh University

in Candidacy for the Degree of

Master of Science

in

Department of Metallurgy and Materials Engineering

Lehigh University

1980

CERTIFICATE OF APPROVAL

This thesis is accepted and approved in partial fulfillment of the requirements for the degree of Master of Science.

16 Sept 1980
(date)

Professor in Charge

Chairman of Department

ACKNOWLEDGEMENTS

I wish to extend my genuine appreciation to Dr. J. I. Goldstein for his encouragement and guidance during my stay at Lehigh. His positive attitude towards research has given me greater confidence in myself. I would also like to thank Dr. R. W. Kraft for his useful suggestions and helpful discussions.

Special thanks are due to Mr. Doug Bush and Ms. Gay Deamer who spent several hours helping me master the operation of the microprobe. Help extended by 'Dr. Al' with some aspects of the probe is also appreciated.

I wish to thank the honorable members of the Zoo--Steve, Paul, Rick, Gay, Dilip and Betty for their enlightening discussions both technical and non-technical (gossip). We spent hours on end frequenting our hangouts and engaging in our favourite past-time--that evil fluid!

My acknowledgements would be incomplete if I do not thank Louise and DeeDee for their patience and understanding and without whose help this thesis would never have seen daylight. Their assistance is truly appreciated. Thanks are also due to John Space Speer for his useful lackey work.

Finally, I would like to thank the Department of Metallurgy and Materials Engineering for extending its facilities during the course of my work.

Financial support from NASA grant #NGR 39-007-043 is acknowledged.

TABLE OF CONTENTS

LIST OF TABLES

LIST OF FIGURES

ABSTRACT

The purpose of this research was to understand how the fractionation trends of trace elements in Fe-Ni meteorites develop using experimental techniques and computer modeling. Plane front and dendritic growth experiments were performed in the laboratory. These results along with the predicted thermal history of parent meteorite bodies indicate that iron meteorites solidify dendritically rather than with a plane front and that fractionation trends are controlled by this process. Therefore Fe-Ni-X alloys, where X is a third element, were solidified dendritically and the composition data from the bulk alloy and the dendrite cores were used to calculate the partition coefficients K_D^X of the ternary elements. These K_D^X values were corrected for solid state diffusion using a modification of a model developed by Flemings et al. (1970). The corrected equilibrium partition coefficients are 0.43 for Au, 0.58 for Ge, 0.12 for P, 0.87 for Ni, 1.45 for Pt and 1.73 for Ir. The diffusivities of Au and Ge, in Fe-Ni, as a function of temperature were measured and used as inputs to the model to account for solid state diffusion.

Further experimentation indicated that K_D^X values can be influenced significantly by elements that depress the melting point. Several meteorite groups such as the IIIABs contain as much as 1 wt% P, an element that depresses the melting point of Fe-Ni alloys. Because Ge varies directly and indirectly with

Ni content in some meteoritic groups, the effect of P on K_D^{Ge} was studied. The experimental results show K_D^{Ge} increasing sharply from 0.58 to more than 1.0. The K_D^{Ge} exceeds 1.0 at 0.5 wt% P in the solid. The variation of K_D^{Ge} with P content or melting point was incorporated into a model which simulates the fractionation behavior of Fe-Ni dendrites containing P and Ge. Such a model explained the positive slope of group IVA and the slope reversal in group IIIAB. Preliminary experiments with S indicate that $K_D^{Ge} >> 1$. This result can be used to explain the negative Ge-Ni slopes of groups I, IIIAB and IIICD.

INTRODUCTION

Over the years a large number of meteorites have been found on the surface of the earth. In order to conduct an organized study these 1700[1] or more meteorites were classified. A very broad classification yielded four basic types of meteorites: chondrites, achondrites, stony-irons and iron meteorites.[2] It was further hoped that a more detailed classification would lend some clues to the history and genesis of meteorites. Of special interest to metallurgists are the iron meteorites which are basically Fe-Ni alloys with varying amounts of trace elements. These iron meteorites were classified into groups and subgroups[3-9] based on Ge, Ga and Ir contents and their correlations with Ni concentrations. Figure 1 shows a plot of log Ge vs log Ni for iron meteorites. This chemical grouping shows Ge concentration varying by several orders of magnitude but tending to cluster into specific compositional ranges.[10] This quantized behaviour led scientists to believe that meteorites from a group came from the same parent asteroid. As for the range of compositions within a group, some fractionation process was believed to be responsible.

The purpose of this research was to understand how the compositional trends of trace elements in iron-nickel meteorite groups develop using experimental techniques and computer modeling. There is widespread controversy as to how an initial asteroid bulk composition can lead to the range of compositions for a chemical group. The current Wasson and Scott theory predicts that metallic

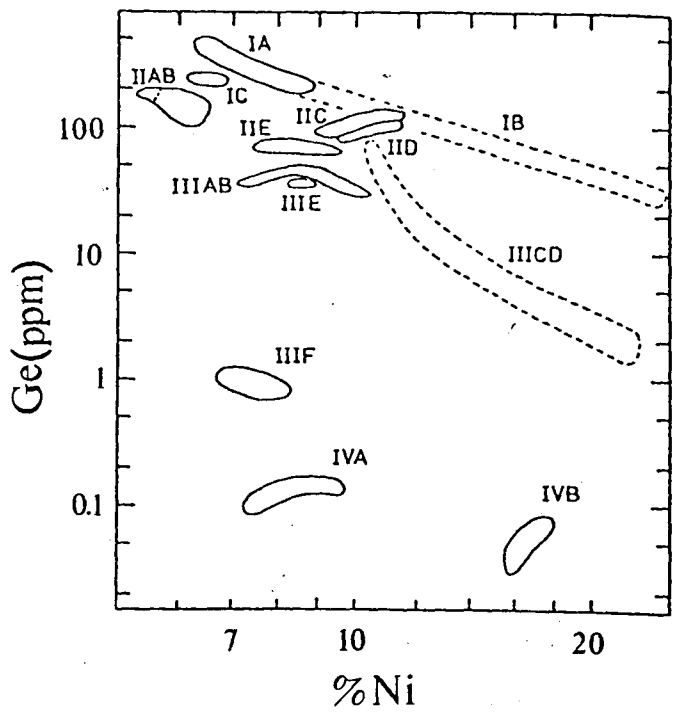

Fig. 1 Chemical grouping of iron meteorites on a log Ge vs. log Ni plot.

cores of parent bodies solidified with a plane front. The partitioning of the elements between the solid and liquid phases during successive stages of solidification is predicted as being responsible for the observed fractionation. Such a freezing mode should result in all groups having approximately the same slope on a log X vs log Ni plot, where X is any trace element. The slope is determined by the partition coefficients (K_D^X and K_D^{Ni}) of the two elements. In the log Ge vs log Ni plot (Figure 1) group IVA has a decreasing positive slope. Group IIIAB exhibits a slope that goes from positive to negative while group I shows a negative slope. The above mentioned groups encompass nearly 70% of all iron meteorites.

The observed Ge-Ni trends are therefore not in agreement with the predictions of the plane front solidification theory. The present work develops a solidification and diffusion model that explains these seemingly inconsistent Ge-Ni correlations. The experiments involve the measurement of ternary partition coefficients of elements in Fe-Ni-X alloys, where X is a third element. This is achieved through cellular solidification experiments and diffusion modeling of the freezing and cooling process in the ternary alloys. In some cases diffusivities were determined by making diffusion couples and using the Matano analysis. Solute-solute interactions during solidification were also investigated and used as inputs to the model.

BACKGROUND

A. Chemical Groups of Iron Meteorites

The discovery of a large number of iron meteorites led to the need for a classification scheme to gain a better insight into these planetary bodies and their probable origins. Over the years several grouping methods have been suggested based on properties such as structure, mineralogy, trace element content, cooling rates, etc. This chapter discusses the chemical grouping of iron meteorites which is based on the trace element contents.

Goldberg et al.[3] in 1951 analysed 45 iron meteorites and divided them into three classes based on major differences in gallium contents and also pointed out that each class had a different structure. In 1957 Lovering et al.[4] studied 88 meteorites and detected the presence of four groups using germanium as an indicator. They also drew attention to the fact that each of their groups corresponded to the previously determined gallium groups. They further confirmed that individual meteorites are essentially homogeneous provided the samples were large enough to give representative portions of both kamacite and taenite. In early 1967 Wasson,[5] in his first of a series of papers, examined 34 iron meteorites which had very low Ga-Ge contents and had earlier been classified as group IV. Using a more sensitive technique he found that it was possible to subdivide this group into IVA and IVB based solely on Ga-Ge concentrations.

In his second paper[6] he examined 64 group III meteorites and resolved them into subgroups IIIA and IIIB. The basis for this resolution was threefold:

i) Mean Ga-Ge content of IIIA was greater than that of IIIB.

ii) There was no overlap of Ni contents between the subgroups.

iii) Group IIIA had a positive correlation between Ni and Ge contents while group IIIB meteorites showed a negative correlation.

In the same paper they reported new members to groups IVA and IVB. Later in 1960 and in 1970 Wasson et al.[7,8] split up group II and group I meteorites. Analyses of 61 group II meteorites resulted in subgroups IIA, IIB, IIC and IID. This subdivision was on the basis of Ni contents, correlations between Ga, Ge and Ir contents and to some extent on structures. The group I meteorites ended up being resolved into I-An 1, I-An 2 and I-An 3. Wasson further comments that these group I meteorites are probably one of the most primitive groups of iron meteorites. In 1971 Wasson and Shaudy[9] further introduced groups IIIC and IIID.

As has been pointed out earlier, one of the main reasons for establishing a detailed and elaborate classification scheme lies in trying to understand and extract some information about the probable origins of meteorites. Although Ge concentrations in

iron meteorites vary by a factor of 14000[5] there is a distinct tendency for them to cluster into specific composition ranges. This "quantized" behaviour seems to imply that members of a Ga-Ge group are probably genetically related. This view was first presented by Goldberg et al. in 1951,[3] who mentioned that each Ga-Ge goup was probably associated with a different parent body. This assumption was further strengthened by cooling rate studies and electron microprobe measurements made by Wood,[11] Goldstein and Short,[12,13] Reed,[14] and Goldstein and Ogilvie[15] which clearly echoed similar thoughts about genetic significance. Although Wasson et al. divided the basic groups into subgroups they believed that meteorites of a group are co-genetic with evidence seeming to favour their origin in the same parent body. The genetic significance of groups IIIA and IIIB will be discussed in greater detail in a later part of this thesis. A standard way of showing these different groups is on a log Ge vs log Ni plot as shown in Figure 1. This plot brings out the compositional trends associated with the different groups. Group IVA exhibits a positive decreasing slope. Group IIIAB shows the slope going from positive to negative and group I has a negative slope. This anomolous behaviour of germanium concentrations has not been fully understood. A part of this thesis will be devoted to developing a model that explains this seemingly inconsistent behaviour of germanium.

B. Fractionation Theories in Iron Meteorites

The fact that Ge concentrations in iron meteorites differ by over four orders of magnitude and yet fall into four distinct groups seems to indicate the occurrence of one or more fractionation processes that need to be explored. The fact that each group or subgroup shows a definite correlation between Ni and Ge concentrations seems to indicate that at least two fractionation events had taken place; one being responsible for fractionation between groups and the other for fractionation within a group.[16]

B.1. Fractionation between groups

Although a lot of work has been done on the primary fractionation of chondritic meteorites not too much work has been done regarding fractionation of iron meteorite groups. Scott[16] points out that this is because the similarity of irons to chondrites has only recently been recognised. Wasson and Wetherill[18] indicated that the chief nebular processes that seem reasonable are fractional condensation and selective accretion. Anders[19] explained the condensation and accretion in planetary bodies with a two component model. Later in 1977 and 1978 Kelly and Larimer[20] and Sears[21,22] used the accretion mechanism to explain the volatile abundance in iron meteorite groups. They determined the temperatures and pressures of accretion by comparing the average compositions of the iron meteorite groups with those for metal grains cooling in equilibrium with the nebula. At present the accretion model has only been tested for a few elements. Wasson

and Wai[23] feel that irons and chondrites experienced similar volatile fractionation and they favor a gas-dust fractionation process. Scott[24] warns that although these models have had some success in explaining the broad trends among iron meteorites, no detailed conclusions can yet be drawn.

B.2. Fractionation within a group

It is believed that the fractionation models described above were responsible for the formation of different asteroids, each with a different homogeneous bulk composition. The different bulk compositions of the asteroids would correspond to the average compositions of the different chemical groups of iron meteorites. These homogeneous asteroid parent bodies, later cool and solidify resulting in the segregation of the trace elements. A subsequent break up of such an asteroid[25] could lead to meteorites coming from different parts of a segregated mass. This is predicted to be the cause for fractionation within groups.

Several theories have been proposed to explain how a homogeneous parent body could segregate during cooling and solidification. Kelly and Larimer[20] have documented these theories in detail. Listed below are some of these theories:

i) Fractionation between metal, silicate and sulphide phases in parent bodies.

ii) Melting/gravitational segregation.

iii) Oxidation and sulfurization.

iv) Fractional crystallisation of the liquid iron core.

Of all these theories the fourth, namely the fractional crystallisation of the liquid iron core, seems to be the most favoured one. This "state of the art" theory predicts that the homogeneous asteroid would, at some point during cooling, have a silicate shell around a molten metallic core. This liquid iron-nickel core then solidified with a plane front. The zonation that results from a plane front solidification is given by the Scheil equation.[26]

$$C_S = K_D^X * C_O * (1 - f_S)^{(K_D^X - 1)} \qquad (1)$$

where C_O is the bulk composition at the start, K_D^X is the partition coefficient of an element X, f_S is the fraction solidified at any instant and C_S the composition of the solid at the solid/liquid interface at that instant. The derivation for this profile assumes thorough mixing in the liquid and no solid state diffusion. For a system that exhibits $K_D < 1$, the solid that forms during successive stages of freezing is increasingly rich in the solute. The resulting frozen solid would thus exhibit a zonation from start to finish. Figure 2 is a representation of the Scheil equation for different values of K_D.[27] The figure shows the solute concentration increasing with the fraction solidified for $K_D < 1$ and decreasing with the fraction solidified for $K_D > 1$. The figure also indicates that for elements with K_D very different from unity, the compositional spread due to solidification can extend over one order of magnitude or more.

Based on this fractionation theory, Scott[16] studied the

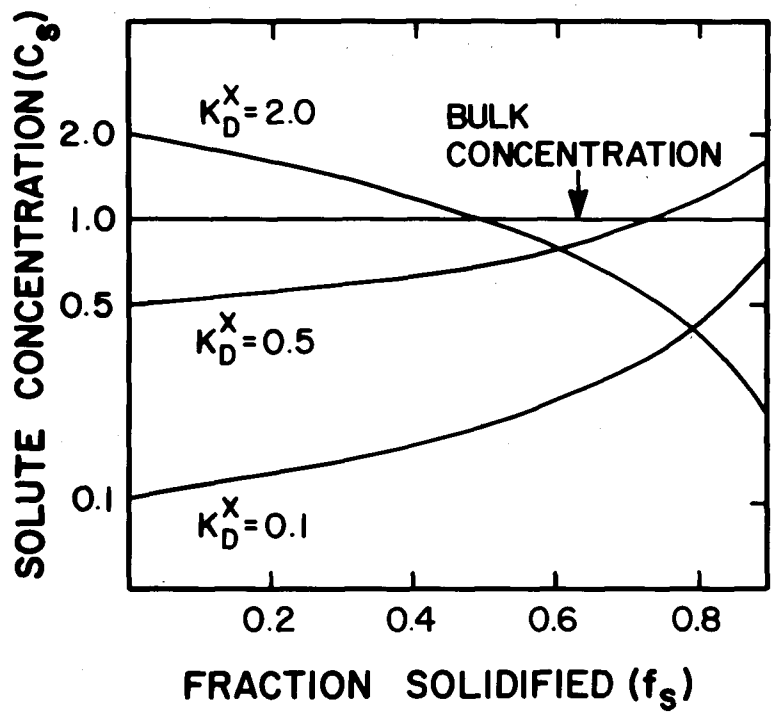

Fig. 2 - Graphical representation of the Scheil Equation.

trends of a number of trace elements in different chemical groups. Using the Scheil equation for both Ni and a third element X, he showed that a plot of log C_S^X vs log C_S^{Ni} would yield a straight line having a slope of $(K_D^X - 1)/(K_D^{Ni} - 1)$. He drew least squares straight lines through the meteorite compositions of each group on a log X vs log Ni plot and assuming $K_D^{Ni} = 0.9$ he calculated the K_D^X values for the trace elements. Table 1 lists the K_D^X values that he reported. In his concluding remarks Scott points out the difficulties faced by this theory. Drawing attention to Figure 1 he points out that group IV and group I have opposite trends. Group IIIAB shows a reversal of trend midway through the group. In view of the fact that the Ge-Ni correlations do not fall in line with the current theory there is a need for a more refined theory. In the latter part of this thesis a single solidification theory will be developed that will explain the different trends seen in the chemical groups.

C. Solidification Theory and Practice in Iron-Base Alloys

C.1. Ternary equilibrium partition coefficients

Ternary single phase alloys, like binary alloys, can be solidified with a plane front provided the thermal gradient is high and the growth rate low.[28] Coates et al.[29] have showed that the same concept of constitutional supercooling can be applied to ternary alloys. The only complication being that the solidus and liquidus are now surfaces and solute-solute interaction may now be important. Taking the Fe-Ni-X ternary alloy as an example,

Element	Partition Coefficients K_D^X			
	Goldstein & Friel	Bild & Drake	Scott	This Study
Ni	0.88	0.78-0.94	0.9	0.87
Ge	0.77	--	---	0.58
Au	0.64	0.18	0.50	0.43
P	0.44	--	0.17	0.12
Pt	1.27	0.90	1.74	1.45
Ir	2.1	--	3.44	1.73
Ce	--	--	---	0.14*

*K_D^{Ce} is not corrected for solid-state diffusion.

Table 1 - Comparison of partition coefficients.

the liquidus temperature will now be dictated not only by the Ni concentration but also the concentration of the third element X. The ternary equilibrium partition coefficient of element X (K_D^X) can now be defined as

$$K_D^X = C_S^X / C_L^X \qquad (2)$$

where C_S^X = concentration of X in solid Fe-Ni

C_L^X = concentration of X in molten Fe-Ni in equilibrium with the solid

The need for ternary coefficients is explained in the following subsections.

C.2. Experimental determination of K_D^X

In order to mathematically model the fractional crystallization theory proposed by Scott[16] to explain the trace element variations within a group, it was necessary to experimentally determine the equilibrium ternary partition coefficients of the concerned elements in solidifying Fe-Ni melts. Two research groups have undertaken this experimental task.[30,31] They adopted two entirely different methods of estimating these partition coefficients. Their approaches to the problem are discussed below and their results are tabulated (see Table 1).

(a) In 1978 Goldstein and Friel[30] conducted planar front growth experiments in the laboratory with Fe-Ni alloys containing small amounts of a third element X. They unidirectionally solidified their Fe-Ni-X alloys by controlling the thermal gradient and the growth rate in a manner that resulted in a planar

solid-liquid interface moving from the bottom to the top of the sample. They then employed an electron microprobe to monitor the concentrations of Ni and X as a function of the distance from the starting interface. Assuming no solid state diffusion together with complete mixing in the liquid they used the Scheil equation (Eq. 1) to fit their experimental profile. Plotting log (C_S^X / C_O^X) vs log $(1 - f_S)$ gave them log K_D^X as the intercept at $f_S = 0$. They also took into account the effects arising from the presence of a narrow diffusion layer[28] ahead of the moving interface. The corrected K_D^X values that they reported are presented in Table 1.

(b) In the same year Bild and Drake[31] attempted equilibrium experiments to find the equilibrium partition coefficients of elements in Fe-Ni alloys. They held Fe-Ni-X alloys of known compositions for over 15 hours, at temperatures that put them in two-phase solid + liquid fields and then quenched the samples. The solid transformed to martensite and the liquid solidified as dendrites. They measured the composition of the solid and the average composition of the liquid and calculated K_D^X by taking their ratio. The results they came up with are tabulated in Table 1. The authors however warn that their study was preliminary and do not advocate the use of their K_D^X values in modelling. The main reason for their hesitation arises from the author's uncertainty of having approached equilibrium. However they do expect to confirm a close approach to equilibrium.

The two attempts to determine partition coefficients described above are among the first that try to determine,

experimentally, the ternary equilibrium partition coefficients.

C.3. Transition from plane front to dendritic growth

The fractional crystallisation theory that has been described earlier assumes a planar solid-liquid interface. Considering the importance of the interface morphology a discussion of the stability of an interface is in order. Ahead of a moving interface is a solute enriched layer. At the interface, the composition is that given by the equilibrium phase diagram (Fig. 3a). The solute concentration decreases as we move away from the interface as seen in Figure 3b. Based on the solute concentration, a plot of the liquidus temperature as a function of the distance from the interface can be deduced from the phase diagram and is shown in Figure 3c. By superimposing the actual thermal gradient over this liquidus profile, inferences about the stability of interface can be drawn. Figure 3c shows a limiting case where the planar front is still stable. Any external gradient less than this would lead to a region where the actual temperature is less than the liquidus temperature giving rise to a zone of constitutional supercooling,[32] shown in Figure 3d. In such a case any proturberance that develops on the interface would see itself in a supercooled surrounding and will be stabilised. This would represent the onset of the breakdown of the plane front growth. Later in 1961 Hucke et al.[33] developed a quantitative criterion for the breakdown of plane front growth. Their theory predicted that the planar interface would be stable if

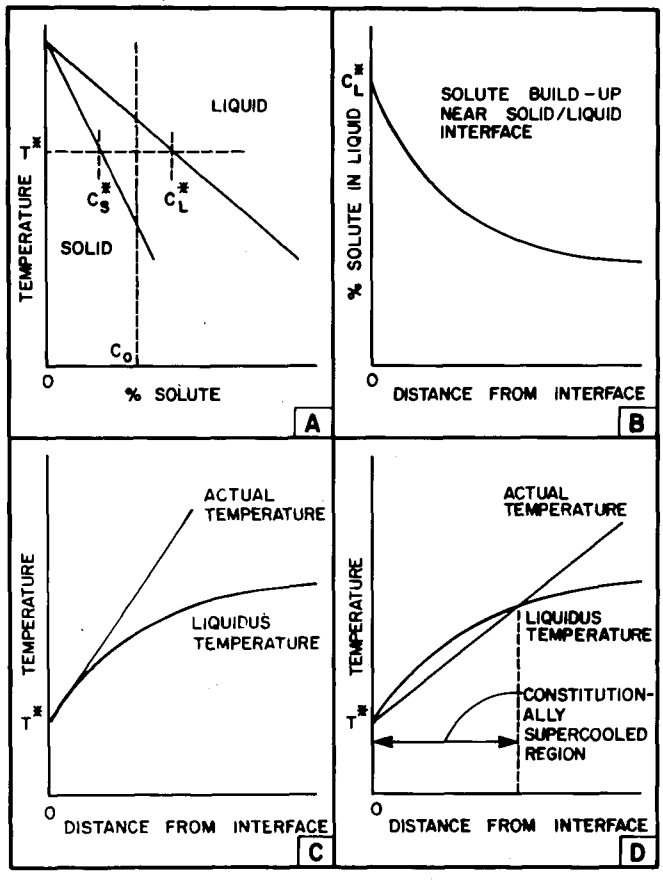

CONCEPT OF CONSTITUTIONAL SUPERCOOLING

Fig. 3

$$\frac{G_L}{R} \geq - \frac{m_L C_S (1 - K)}{K D_L} \qquad (3)$$

where G_L = thermal gradient in the liquid ($^{o}C/cm$)

R = growth rate (cm/sec)

m_L = slope of the liquidus line ($^{o}C/wt\%$)

C_S = solute concentration at the interface (wt%)

K = equilibrium partition coefficient

D_L = diffusivity in the liquid (cm^2/sec)

For any value of G_L/R less than that predicted by this equation a cellular growth would result. At an even greater growth rate or a lower thermal gradient these finger-like cells begin to develop secondary arms. These are commonly referred to as dendrites. Figure 4 shows a typical cellular growth and can be referred to as primary dendrite arms. This Fe-Ni-Ce alloy was grown with a G/R ratio below the critical value. The finger-like structure represents the cells growing along the direction of interface motion.

C.4. Solute redistribution during dendritic solidification

In the early 1950s Rutter and Chalmers[32] showed qualitatively that during cellular solidification the solute concentration at the center of the cell is different from that at the cell edge. The problem of modelling such a solute redistribution becomes, as indicated by Flemings,[28] extremely complex for a number of reasons, some of them being:

a) Multidimensional diffusion

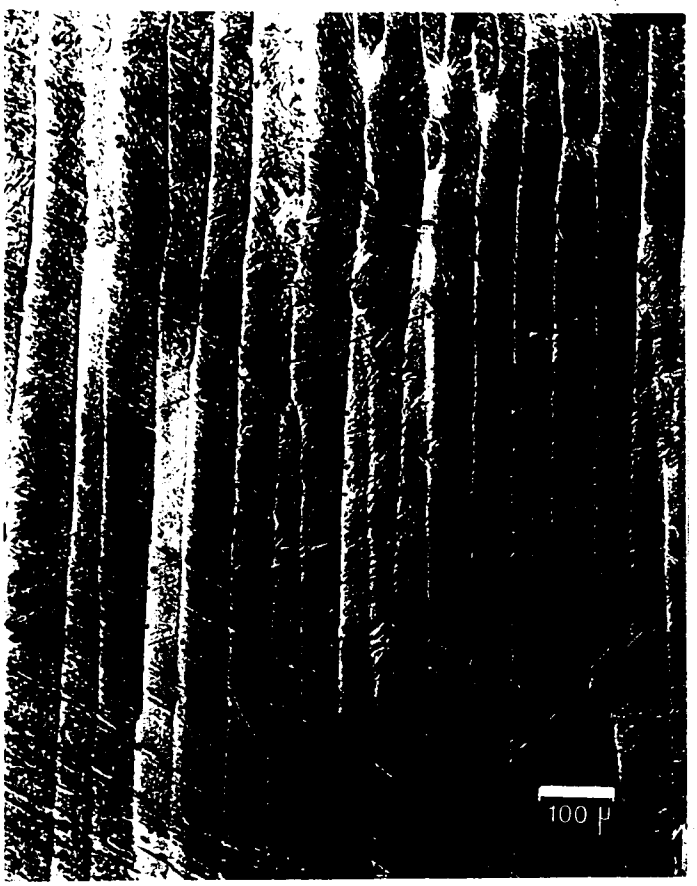

Fig. 4 - An example of cellular growth.

b) Effects of radius of curvature at cell tips.

The process of modelling can however be simplified by making some suitable assumptions. Brody and Flemings[34] proposed a plate-like dendrite morphology with the plates parallel to the heat flow direction. Figure 5 shows the dendrite plates and the selection of a suitable volume element to characterize solute redistribution. Within this volume element the dendrite wall moves from one end to the other and the Scheil equation (Eq. 1) can, as before, be used to describe the segregation. This model is based on the following assumptions:

i) There is negligible undercooling before nucleation or from curvature of cell tips.

ii) There is no mass flow in or out of the volume element.

iii) Diffusion in the liquid is complete.

iv) The equilibrium partition coefficient K_D is a constant for that solidification and applies at the interface.

v) Diffusion in the solid is negligible.

Figure 6 shows a Ni profile based on Brody's model with no solid state diffusion. A Fortran program was written to see how well the numerical technique compares with the analytical Scheil equation. However microsegregation sets up concentration gradients between cell centers and cell edges. This differential solute content forces the solute atoms down the concentration gradient in an effort to flatten the profile. This solid state diffusion effect could become appreciable for some elements if the temperature is high enough and/or the time long enough. There

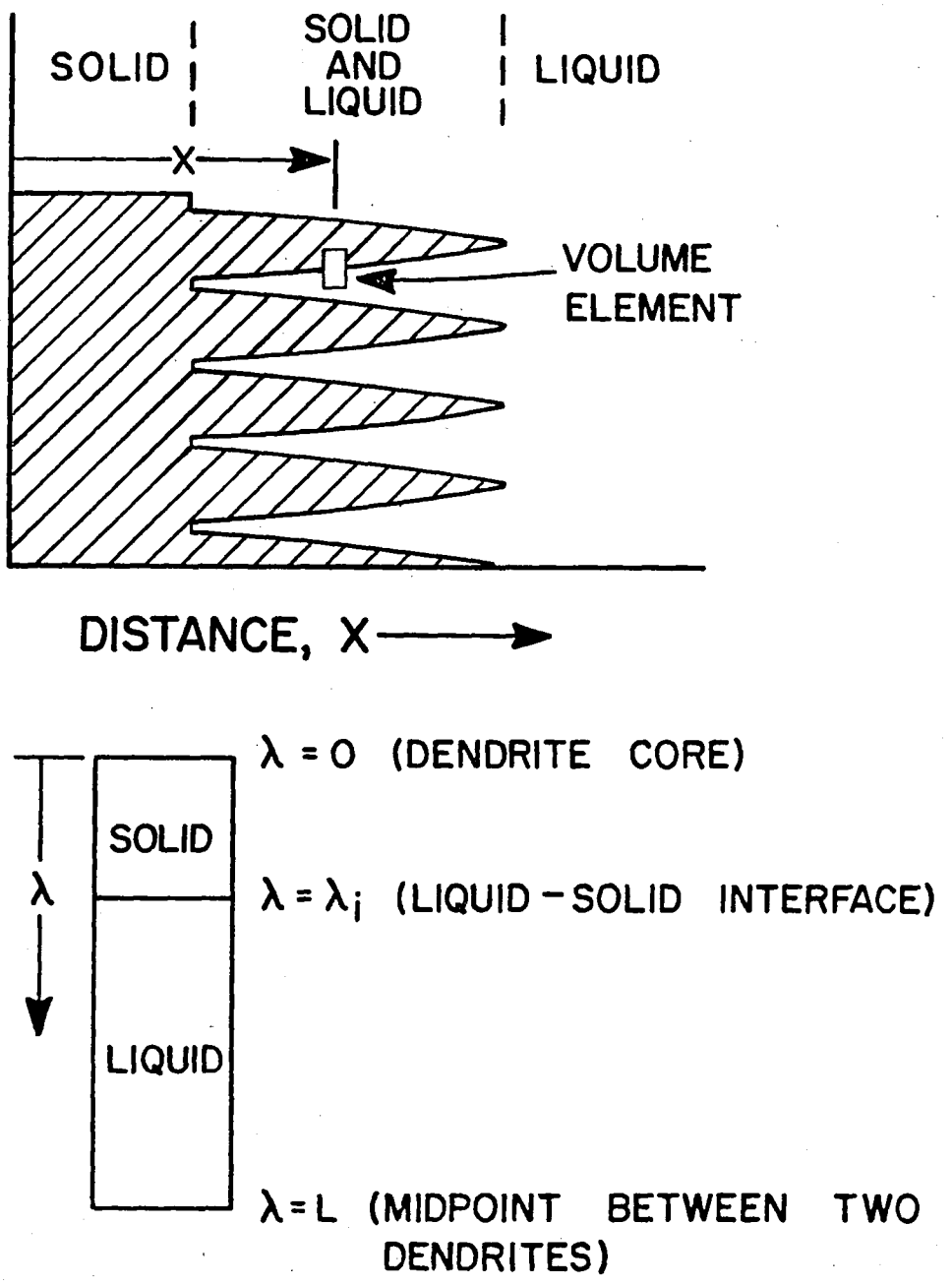

Fig. 5 - The dendrite plate model showing the volume element.

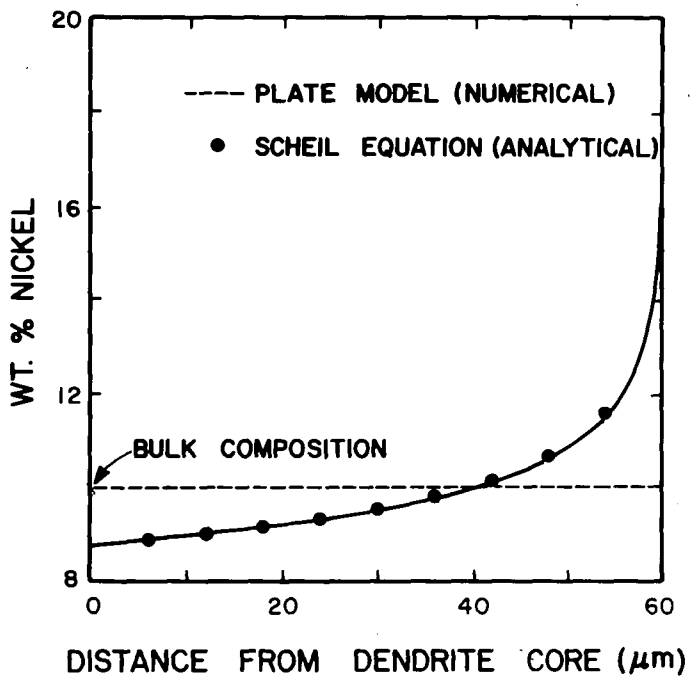

Fig. 6 - Nickel segregation profile generated by the model.

are two stages of diffusion that need to be considered.

i) Diffusion during solidification in the solidified portion.

ii) Diffusion during subsequent cooling to ambient temperatures.

The diffusion effects can easily be incorporated into Brody's model. Flemings et al.[35] have described in detail a numerical technique, based on Brody's model, that calculates segregation profiles taking into account the solid state diffusion effects. The details of the computing technique will be discussed later under the experimental techniques section.

EXPERIMENTAL PROCEDURE

A. Experimental Design

This thesis has two main areas of emphasis. The first is to dendritically solidify Fe-Ni-X alloys and study the microsegregation behaviour of the third element X. In order to accomplish this, bulk alloys of Fe-Ni-X were induction melted from pure elements and the melt was withdrawn from the induction coils under a thermal gradient at a predetermined rate to ensure dendritic solidification. The electron microprobe technique was then employed to investigate the segregation behaviour. The effect of solid state diffusion, on the segregation profile, was studied and incorporated to yield the equilibrium partition coefficients that were responsible for the microsegregation. The diffusion calculations required the knowledge of diffusivities of elements as a function of temperature. In cases where diffusivities were not documented, they were determined by making diffusion couples and employing the standard Matano analysis.

The second area of emphasis is to study the effect of P, an element that lowers the melting point of Fe-Ni alloys, on the partitioning behaviour of germanium. The results of the experiments are then used to explain the different correlations between Ge and Ni in the different chemical groups. The experiments for this study involved holding an alloy of a given composition in two-phase field for a sufficient period of time to establish equilibrium and then quenching them to retain the liquid

composition. The electron microprobe was used to obtain compositional data from the samples.

B. Preparation of Bulk Alloys

All alloys were made up using pure elements. Most trace elements in meteorites are in the ppm range and this would be an ideal trace element concentration for the experimental alloys. However, reliable and reproducible quantitative data from the microprobe demands much higher concentration levels. Because this condition puts a lower limit on the ternary additions most alloys had about 1% by weight of the third element. The iron and nickel together made up $\sim 99\%$ of the alloy. Fe and Ni were obtained in the form of 5 mm diameter rods from United Mineral Corporation, New York. The composition information for iron and nickel is given in Table 2. The third element that made up $\sim 1\%$ of the alloy was in the form of either chips, powder or wire. Pertinent information is given in Table 3. The required amounts of the elements were cut and weighed and placed in a mullite crucible (Coors Porcelain, Colorado). The crucible was then placed within the induction coil of a 15 kw 3-phase thermonic radio frequency generator. Figure 7 is a schematic representation of the experimental set up. The crucible was flushed with a mixture of argon and hydrogen (20:1) for a couple of minutes to ensure that the sample did not see an oxidising atmosphere during the melt. With the controlled atmosphere around the sample the generator was turned on. The heating was controlled to avoid the failure of the crucible from thermal shock. The molten metal was

	Si	Cu	Fe	Mn	Mg	C
Fe*	5	2	solvent	5	2	70
Ni*	<1	2	15	-	<1	9

*United Mineral Corp., New York.

Table 2 - Purity of iron and nickel.
(Impurity levels in ppm)

Ternary addition	wt% in alloy	Form	Purity
Ge	1%	Pieces	50 ohm-cm*
Au	1%	Wire	24 carat
P	up to 3%	Red powder	99% + (t)
Pt	1%	Wire	99.9% + (m)
Ir	1%	Wire	99.9% +
Ce	1%	Chips	99.9% +

m: purity based on metallic content
t: purity based on total contaminants
*: purity in terms of electrical resistivity

Table 3 - Purity of ternary additions.

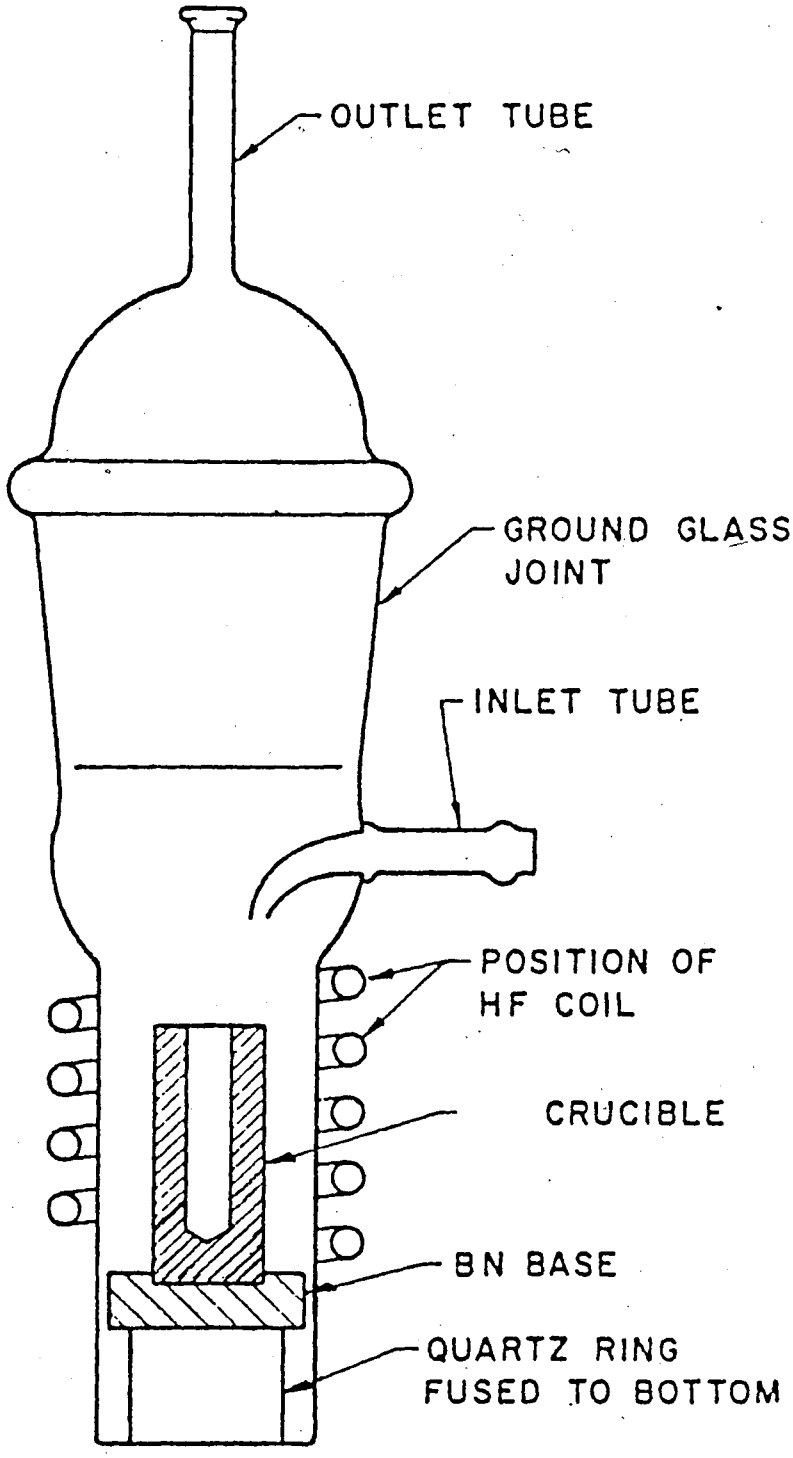

Fig. 7 Vertical induction furnace set up.

maintained above the liquidus for 3-5 minutes to allow for complete mixing. The sample was then cooled slowly and this yielded a reasonably sound sample free from porosity. The vapour pressures of elements in solution were low enough that any loss by vaporization could be ignored.[37] In the case of phosphorous there was a significant loss during the initial heating cycle but this was compensated for by addition of extra phosphorous at the start. Once the P goes into solution it is observed that there is no further loss.[37] Addition of P into molten Fe-Ni also helped conserve P and assure better control over the bulk P content.

C. Directional Solidification Experiments

The bulk alloys that were used for directional solidification experiments were made up as described above. The alloy was put into a mullite crucible and placed inside the induction furnace coils as before (Fig. 7). The bottom of the crucible now rested on a crucible holder which could be moved relative to the coils with a variable speed motor. There was provision for spraying water onto the bottom of the crucible. Suitable refractory spacers were used to position the alloy within the coils. The protective atmosphere was then let in and the generator was turned on. After most of the alloy was molten the motor was turned on and the crucible was gradually withdrawn from the coils. This experiment was repeated several times with different samples at different withdrawal speeds to detect the critical growth rate where the plane front growth would breakdown. Figure 8 shows a plane front growth below the critical growth rate and Figure 9 shows a cellu-

Fig. 8 - Plane front growth below critical growth rate. This alloy was grown at 5.75 cm/hr. which is below the critical rate of 6.0 cm/hr.

Fig. 9 - Cellular growth above critical growth rate. This alloy was grown at 6.43 cm/hr. which is above the critical rate of 6.0 cm/hr.

lar growth pattern above the critical growth rate of 6 cm/hr. The breakdown is governed by the G/R ratio described in equation 3. A growth rate of $\sim$ 10 cm/hr was then chosen for the experiments which ensured a cellular growth. Although all segregation experiments were done with $\sim$ 10 cm/hr growth rates, some experiments were done at higher growth rates to see the effect on dendrite spacing/cell size.

D. Metallography and Microanalyses of Directionally Solidified Alloys

The directionally solidified samples were cut longitudinally (parallel to the growth direction) and mounted in lucite. The specimens were then carefully ground through to 600 grit paper. This was followed by polishing with 1 μm alumina powder. These polished surfaces were then etched with Marble's reagent for 5-10 seconds to reveal the dendritic substructure. Specimens that had well aligned cells were taken for further analyses. Cells were considered well aligned if the long axis of the cells were within 15^{o} of the growth direction. These samples were then cut transverse to the growth direction and again mounted in lucite. In all cases the mounted longitudinal section was preserved while the other half was used for the transverse sectioning. For microprobe analyses the following preparation steps were used. The 600 grit grinding stage was followed by polishing with 6 μm diamond paste and then with 1 μm diamond paste. Finally a light hand buff with 0.06 μm alumina was used. The surfaces were then

etched very lightly with 1% nital to help locate the areas of interest on the microprobe. Figure 10 shows a typical longitudinal section with well aligned dendrites and Figure 11 shows its transverse section.

The samples for the electron microprobe analysis were coated with a conducting layer of carbon to avoid charging. The details of the operation of the instrument and the correct choice of operating parameters have been explained in great detail.[38] In most cases, since the third element X made up only $\sim$ 1% of the alloy, high sample currents like 0.2 μA were often used. Transverse sections rather than longitudinal sections were used for microanalysis so that the true centers of the dendrites could be located.

Two kinds of microanalyses were obtained:

i) Several point analyses at the centers of cells to locate the core composition (see Fig. 11). In cases where $K_D < 1$ this would be the minimum composition and in cases where $K_D > 1$ it would be the maximum composition. Of all the cell center measurements the one yielding the maximum/minimum composition, as the case may be, was chosen as the core composition.

ii) Several area scans over the cross-sections to measure the average or bulk composition of the surface. In all cases the mean of the scan readings was taken as the representative value.

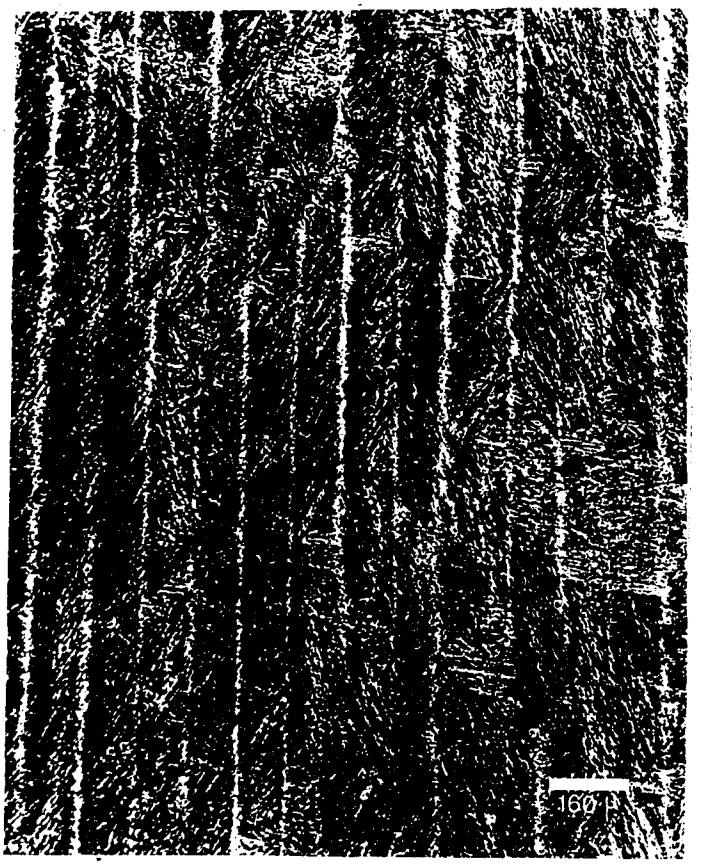

Fig. 10 - Longitudinal section of a dendritically solidified Fe-Ni alloy.

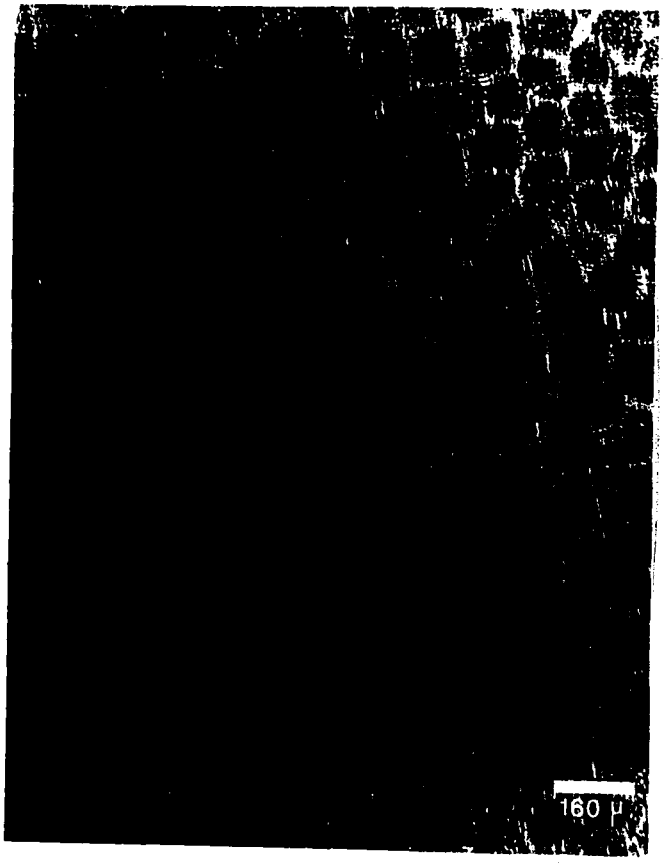

Fig. 11 - Transverse section of the alloy shown in Fig. 10. The cell centers can be easily recognized.

The ratio of the core composition to the average composition gives the experimental partition coefficients K_D^X for the element X (Eq. 2). These K_D^X values were later corrected for solid state diffusion effects.

E. Measurement of Diffusion Coefficients

In order to calculate the solid state diffusion effects on the segregation profiles, knowledge of diffusivities, as a function of temperature, is required. In cases where such information was not documented, experiments were done to measure the same.

Most solidification experiments were concerned with Fe-Ni-X alloys containing $\sim$ 9% Ni and $\sim$ 1% X. The diffusivities of gold and germanium were measured. The experimental technique and choice of end members for the diffusion couples are described for Ge. The same techniques were used for gold.

Two master alloys were made up for the germanium diffusion couples. One had an approximate composition of Fe-9% Ni and the other about Fe-9% Ni-1% Ge. The alloys were made up as described in an earlier section. The alloys were then homogenised so that they would have a uniform composition across any transverse section. This was accomplished by placing the alloy samples in a quartz tube with a piece of tantalum foil as an oxygen getter. The tube was then evacuated and sealed. The capsule was then checked with a Tesla coil to ensure that the evacuation was

adequate. This evacuated tube was then placed inside a horizontal tube furnace at 1200°C for 90 to 160 hours. Homogeneity over the length was not required because the sample was to be used as slices, whose thickness was less than the diameter of the tube. Homogenisation details are given in Table 4. Each alloy was then sliced into discs ~ 2 mm thick. One slice from each alloy was taken for homogeneity studies. To verify homogeneity the samples were analysed in the electron microprobe. Twenty-one random points were chosen for compositional information. The level of homogeneity[38] for a given $(1 - \alpha)$ confidence level is given by

$$\pm \frac{W_{1-\alpha}}{C} = \pm \frac{t^{1-\alpha}_{n-1}}{\sqrt{n}} \cdot \frac{S_C}{\bar{N}} \cdot 100 \text{ relative \%} \qquad (4)$$

where $W_{1-\alpha}$ is the range of homogeneity, C is the true weight fraction of the element of interest, n is the number of measurements, $\bar{N}$ is the number of counts accumulated during each analysis, S_C is the standard deviation associated with the total counts, $t^{1-\alpha}_{n-1}$ is the student t value and $(n - 1)$ is the number of degrees of freedom. Since Ni is the slowest diffusing species at 1200°C it was assumed that homogeneity with respect to Ni implied homogeneity for gold and germanium. Similar samples with longer homogenization times at 1200°C were automatically assumed homogeneous, see Table 4. A 99% confidence level was chosen.

One slice from each master alloy constituted the end members of the diffusion couples. The two slices for the couple were ground and polished on one side. Polishing was done with 6 μm

TABLE 4. Homogeneity data for diffusion couples

Sample #	Alloy Composition				Homogenisation		Level of Homogeneity
	Ni(wt%)	Ge(wt%)	Au(wt%)	Fe(wt%)	Temperature ^{o}K	Time (sec.)	Relative %
1	9.2	1.05	-	Rest	1473	32.76×10^4	0.29
2	9.2	-	-	Rest	1473	32.76×10^4	0.29
3	11.0	-	1.0	Rest	1473	57.6×10^4	≤ 0.29
4	9.5	-	-	Rest	1473	57.6×10^4	≤ 0.29

and 1 μm diamond paste to ensure perfectly flat surfaces for good diffusion bonding. The two polished surfaces were then mated and placed in a diffusion clamp and pressed together. A schematic representation of the configuration is shown in Figure 12. The diffusion clamp with the couple was then encapsulated in a quartz tube as described before. The diffusion heat treatments were done in a three-zone horizontal tube furnace and the temperatures were monitored with a Pt - Pt 10% Rh thermocouple. The diffusion temperatures and times are given in Table 5. At the end of the heat treatment period the couples were quenched by breaking the quartz tube under water. The couples were then sectioned normal to the interface and mounted in lucite. The surfaces were then polished and coated as described earlier. The concentration profile of germanium across the interface was monitored with an electron microprobe. The operating details are discussed in Reference 39. The analysis involved taking composition data at 6 μm or 10 μm intervals going across the interface. Three independent profiles were taken on each couple. The three profiles were then superimposed and the best curve through the three sets of data was drawn. This 'best-fit' curve was then used for the standard Matano analysis. The interdiffusion coefficient is given by[39]

$$\tilde{D} = -\frac{1}{2t} \cdot \frac{1}{\partial C/\partial X} \cdot \int_{C_1}^{C} X \cdot dC$$

where t is the diffusion time, X is the distance from the Matano interface and C is the concentration at a distance X. The

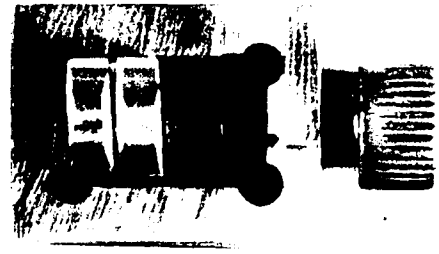

DIFFUSION CLAMP

Fig. 12 - A schematic of the diffusion experiment set up.

	Couple Type	Diffusion Temp (^{o}K)	Diffusion Time (Hrs.)
1.	Fe-Ni/Fe-Ni-Ge	1253.0	62.50
2.	Fe-Ni/Fe-Ni-Ge	1358.0	36.00
3.	Fe-Ni/Fe-Ni-Ge	1493.0	16.00
4.	Fe-Ni/Fe-Ni-Au	1363.0	63.00
5.	Fe-Ni/Fe-Ni-Au	1438.0	25.75
6.	Fe-Ni/Fe-Ni-Au	1463.0	26.25

Table 5 - Diffusion times & temperatures.

graphical integrations were performed on 55 cm x 45 cm graph sheets to minimise computational errors. This analysis at each temperature yielded the interdiffusion coefficient of Ge ($\tilde{D}_{Ge}$) at that temperature. The analysis was done at three different temperatures for germanium and three temperatures for gold as indicated in Table 5.

F. Equilibrium Partition Coefficient Experiments

The main aim, of this set of experiments, was to study the effect of phosphorous on the partition coefficient of germanium. Preliminary experiments were also done to study the effect of S on the partitioning of Ge. In summary, the experiments involved holding Fe-Ni-P-Ge alloys or Fe-Ni-S-Ge alloys at temperatures that put them in solid + liquid two phase fields. Once the phases were in equilibrium the samples were quenched and analysed in the electron microprobe. The details of the experiment follow.

A careful choice of alloy compositions and experimental temperatures were made using the following phase diagrams:

i) The Fe-Ni phase diagram[40] - see Fig. 13.

ii) The Fe-P phase diagram[41] - see Fig. 14.

iii) The Fe-Ni-P low temperature ternary phase diagram[42] - see Figs. 15a and 15b.

Nickel contents were dictated by the fact that compositions should be similar to those of meteorites (5-12% Ni). The Fe-Ni-P ternary phase diagrams reported by Doan and Goldstein[42] indicate the presence of a three phase $\alpha + \gamma$ + liquid field in this Ni

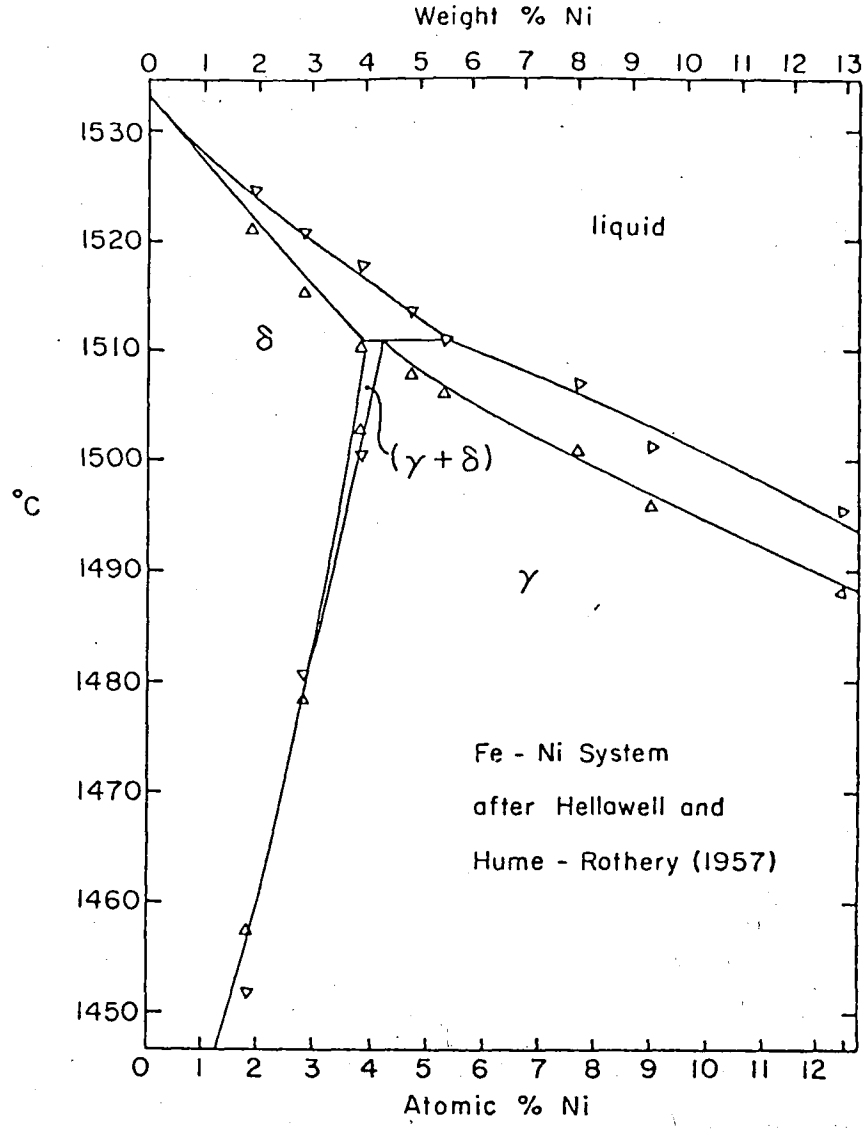

Fig. 13 The Fe-Ni phase diagram at high temperatures.

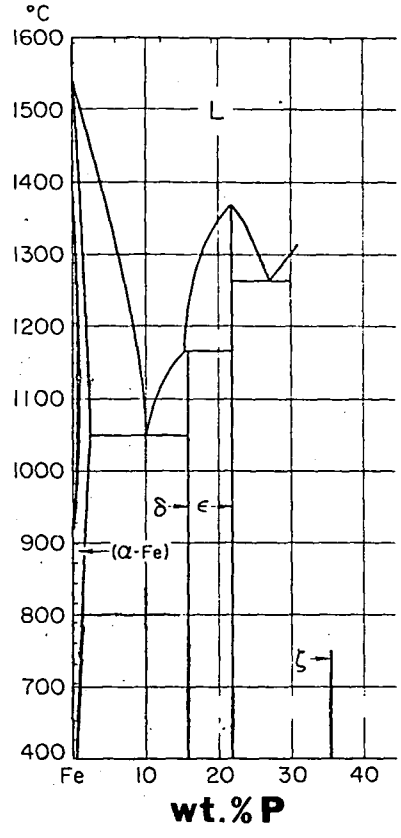

Fig. 14 The Fe-P phase diagram.

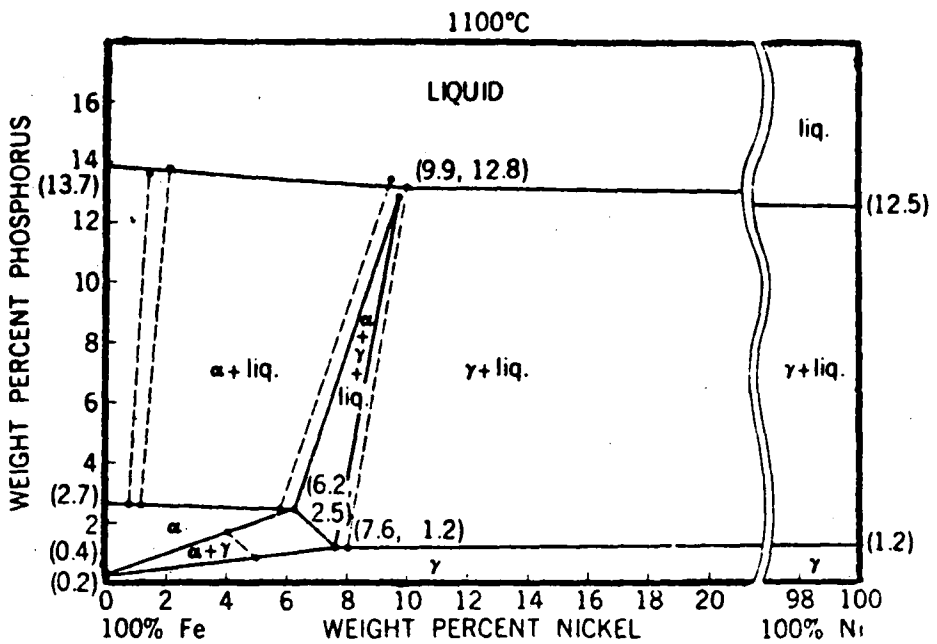

Figure 15a. The Fe-Ni-P ternary phase diagram at 1100°C.

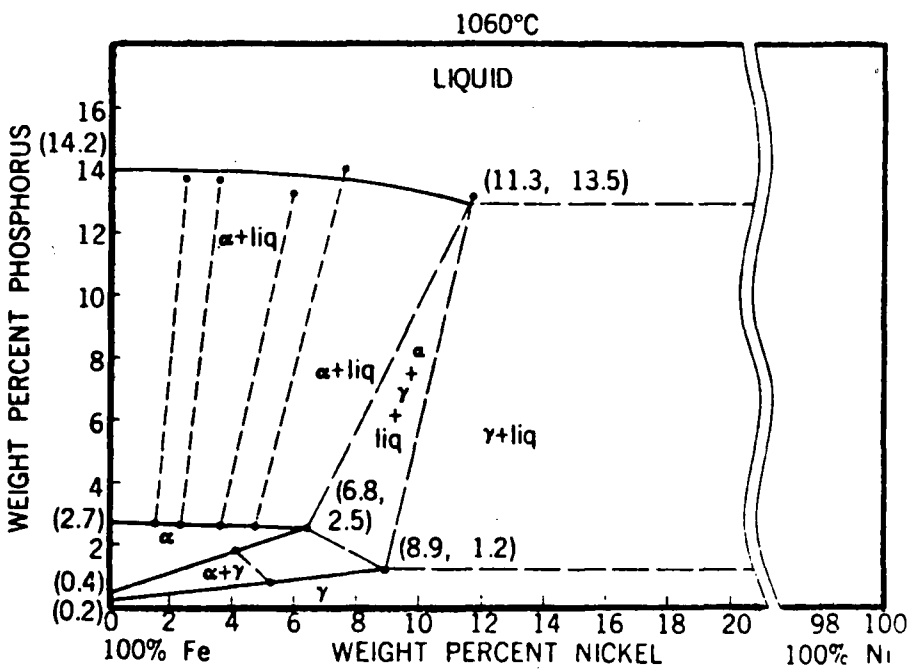

Figure 15b. The Fe-Ni-P ternary phase diagram at 1060°C.

range. The paper also shows the three phase field moving to lower Ni contents at higher temperatures. Although data is available only up to 1100°C the trend seems to indicate that an alloy with ~ 9% Ni would remain in the γ + liquid field from 1100° up to the liquidus temperatures near 1450°C. On this basis an approximate Ni content of 9% was chosen. Germanium levels in meteorites range from a couple of ppm to a few hundred ppm and this would therefore be an ideal range of Ge concentration for the experimental alloys. However, as described earlier, good, reliable quantitative information from the electron microprobe, required for this study, demands much higher Ge levels. Most alloys had between 0.5% and 1% by weight of germanium.

The choice of phosphorous levels and experimental temperatures went hand in hand in that the temperature dictated the phosphorous level. The Fe-P phase diagram proved to be a useful phase diagram for an approximation. The Fe-S phase diagram was used for estimating S contents. Although the exact amount of phosphorous is not critical in determining the phase compositions, the phosphorous level dictates the amount of the phases present. For experimental ease and reliability of the chemical data, a high liquid fraction was desirable. Therefore the P levels used were between 2 and 6% by weight. The P contents were higher at lower temperatures in order to retain a reasonable amount of liquid. About 3 to 4 wt% S was used for the preliminary experiments with S.

The bulk alloy was made up as described earlier. The alloy

was then transferred to an alumina crucible 2.5 cm long and 1.0 cm in diameter (Coors Porcelain, Colorado). The crucible was then placed in a platinum basket and the basket was suspended with a platinum wire in a high temperature vertical tube furnace (Lemont Scientific). A schematic drawing of the setup is shown in Figure 16. Provision was made for passing argon gas through the furnace during the experiment to prevent oxidation of the alloy. A Pt-Pt 13% Rh thermocouple was used for a controlling thermocouple and a similar thermocouple was used to monitor the temperature inside the furnace adjacent to the crucible. The alloys of known compositions were held at the desired temperatures for 2 to 4 hours so that the coexisting phases would reach equilibrium. This was followed by a water quench which involved allowing the crucibles to fall through the furnace into a can of water placed under the furnace. The platinum wire holding the basket was fixed to a stand with a nichrome wire which could be severed every time a specimen needed to be quenched. This was done solely to conserve platinum. The quenched alloys were then sectioned normal to their circular cross section, mounted in lucite and polished as before. The surfaces were etched lightly with 2% nital to reveal the microstructure. Figure 17 shows a typical microstructure where the large grains were the γ grains at the temperature of the experiment while the pool of dendritic structure between the grains was the liquid at the high temperature which solidified as fine dendrites during the quench. If sufficient liquid phase was present, then the solid tended to settle down to the bottom of

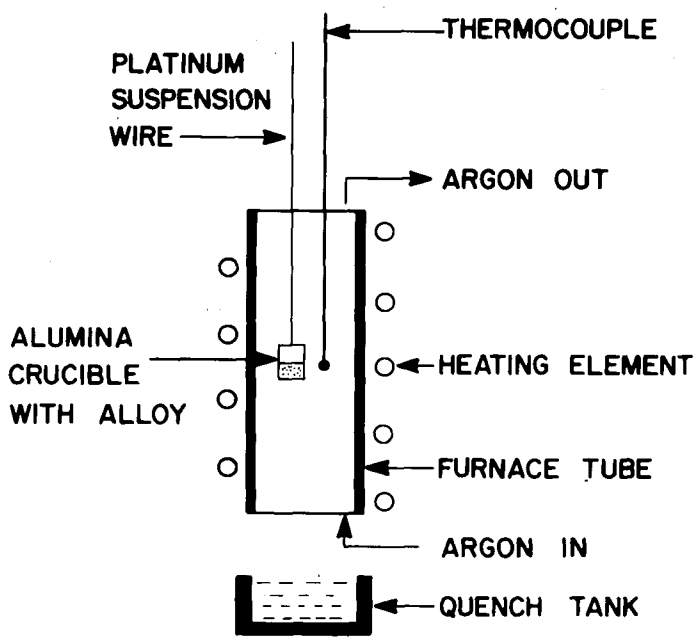

Fig. 16 - A schematic of the vertical tube furnace.

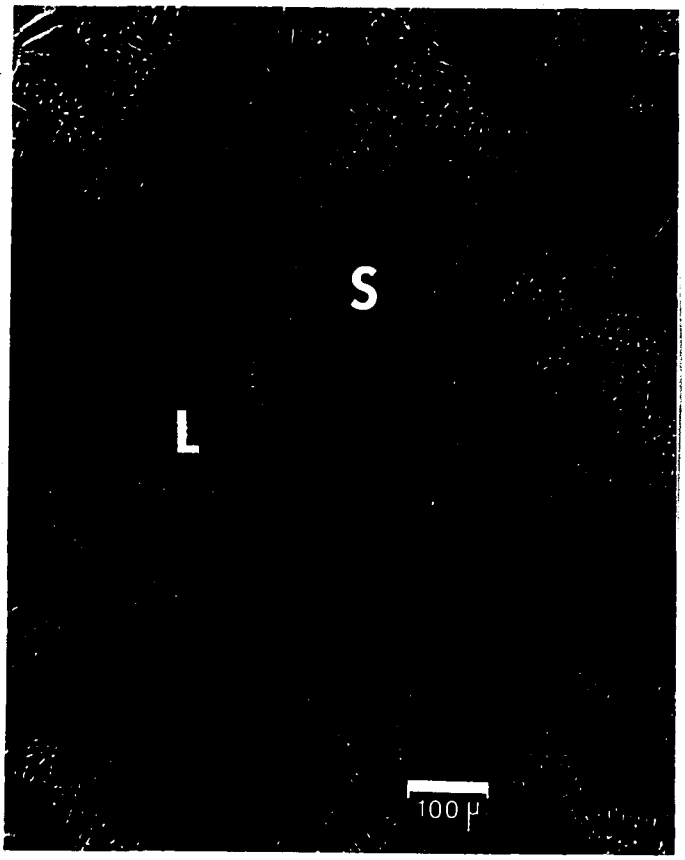

Fig. 17 - A modified solid + liquid structure.

the crucible with the liquid floating on top. Figure 18 shows such a sample where the separation is very effective.

Before the samples were investigated on the electron microprobe they were repolished with 6 μm and 1 μm diamond paste. A very light etch was used to help locate areas of interest on the microprobe. The samples were then coated with a thin conducting layer of carbon as before. The microprobe study of a sample involved acquiring compositional data from the modified solid and liquid phases described earlier. Quantitative analysis was straightforward in that a point analysis on any grain was representative. Analysis of the dendritically solidified liquid phase proved to be a little more involved.

Because of the structure, two kinds of analyses were done. One was an area scan and the other a defocussed beam analysis. In both cases, the choice of a representative area for an analysis was important. The ratio of Ge concentration in the solid to that in the liquid determines the partition coefficient of Ge at the temperature of the experiment. The P level in the solid is also determined by the temperature and K_D^P was also determined.

G. Correction for Solid State Diffusion

The partition coefficients measured in the directional solidification experiments were corrected for solid state diffusion effects. A computer program that simulated the effect of diffusion on dendritic segregation was used. The steps used to correct for solid state diffusion are:

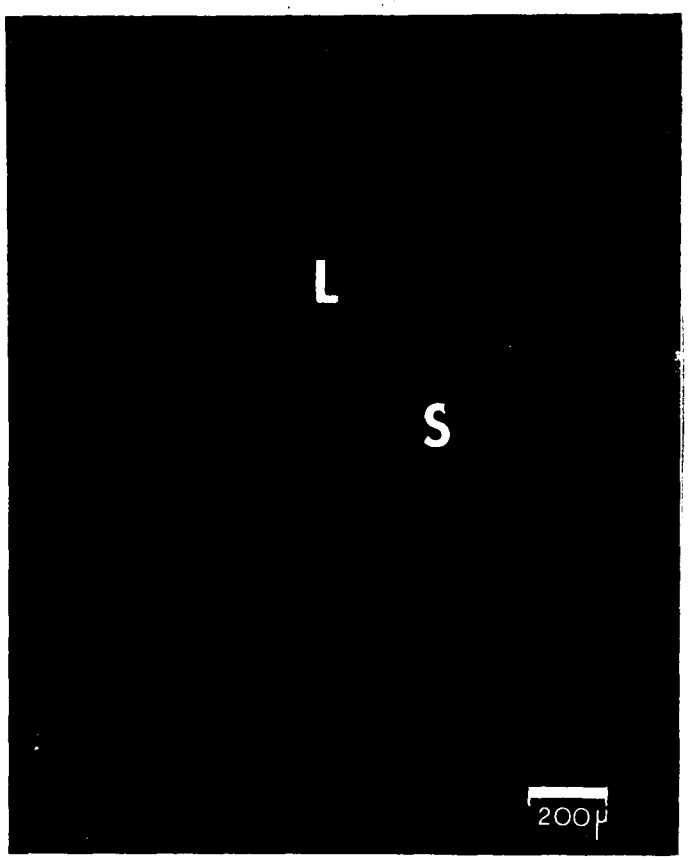

Fig. 18 - An effective solid-liquid separation.

i) Assume an equilibrium K_D^X for the element X.

ii) Calculate the segregation due to this K_D^X.

iii) Incorporate the solid state diffusion effect and note the change in the core composition of the dendrite.

iv) Use the new core composition to calculate the corrected K_D^X.

v) Check to see if the corrected K_D^X matches with the measured partition coefficient.

vi) Repeat these 5 steps until an assumed equilibrium K_D^X gives a corrected K_D^X that approximates the measured partition coefficient.

This correction process is shown schematically in Figure 19. The curve marked 'before diffusion' is the segregation profile developed by the numerical version of the Scheil equation. C_b refers to the dendrite core composition. The curve marked 'after diffusion' shows the change in the segregation pattern due to solid state diffusion. C_a refers to the modified core composition. The dotted line represents the starting bulk composition. Note the change in the core composition due to diffusion. The details of calculating the segregation profile and incorporating the solid state diffusion effects are discussed below.

The numerical technique uses the plate model developed by Brody and Flemings.[57] The assumptions that go into the model

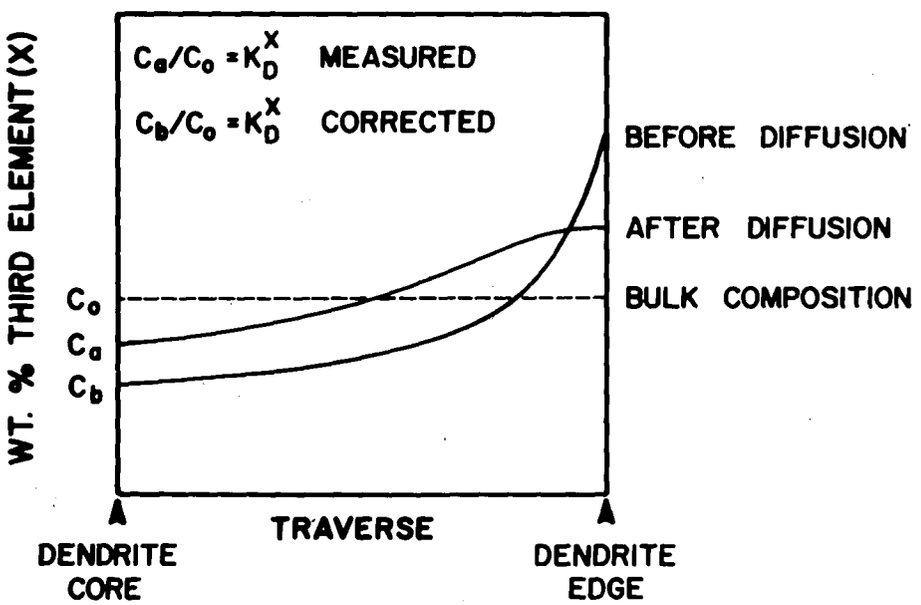

Fig. 19 - A schematic for the correction of K_D^X.

have been discussed earlier. A schematic representation of the model is seen in Figure 5. The figure also shows the volume element chosen for calculating the segregation profile. The volume element has an infinitesimal thickness parallel to the dendrites. The element is divided into a number of layers. At the start, all the layers are molten. With the passage of time the layers solidify successively until all the layers are solid at the end of the freezing process. At any intermediate time, t, each layer, solid or liquid, is assigned an average composition. The concentration of a layer forming at the solid-liquid interface is given by the product of the composition of the liquid and the partition coefficient K_D^X. Following the solidification of every layer, the composition of the liquid is recalculated using a mass balance. Since the model assumes complete mixing in the liquid all the molten layers will have the same average composition. After each stage of solidification, the effect of diffusion in the solidified fraction is evaluated. After the freezing process is complete the diffusion calculations are continued till the temperature has dropped to $1000^{o}C$. The diffusion effects below $1000^{o}C$ are considered insignificant because the sample has a cooling rate of $1^{o}C/sec$. Figure 20 shows a flow chart that outlines the computer program.

The diffusion process can be described by the partial differential equation

$$\frac{\partial C}{\partial t} = \frac{\partial}{\partial X} \left(D \frac{\partial C}{\partial X} \right) \qquad 6$$

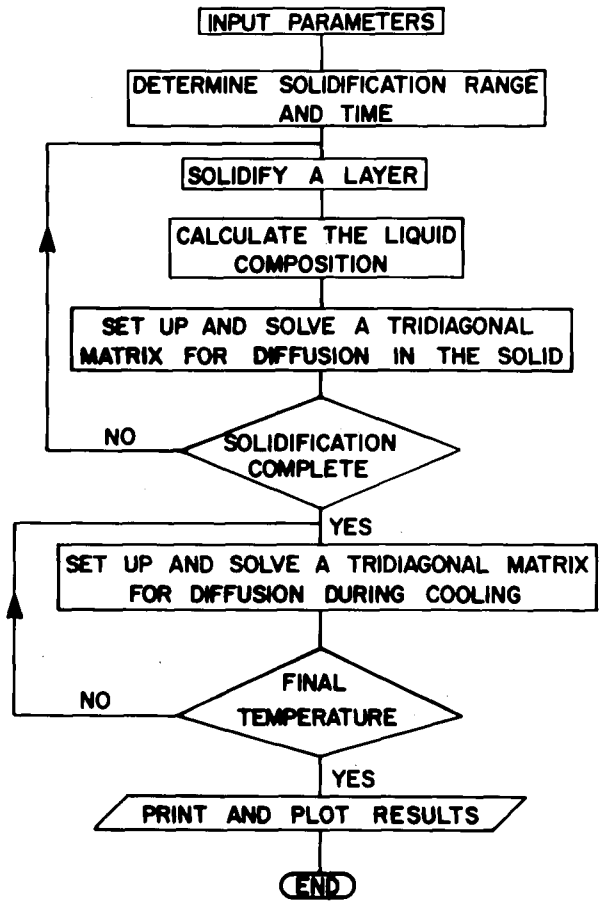

Fig. 20 - A flow chart for segregation calculation.

where $\partial C/\partial X$ is the concentration gradient, D is the diffusion coefficient and t is the time. If D is assumed independent of composition the equation can be rewritten as

$$\frac{\partial C}{\partial t} = D\frac{\partial^2 C}{\partial X^2} \qquad 7$$

In the paper by Brody and Flemings[57] the diffusion effects are calculated by the forward finite difference technique. While the analog for $\partial^2 C/\partial X^2$ is second-order correct that for $\partial C/\partial t$ is only first-order correct. The computer program described in this thesis uses the Crank-Nicolson technique[43] where the analog for $\partial C/\partial t$ is second-order correct. Therefore the program requires fewer time steps. The solid is divided into layers and a space-time grid is set up as shown in Figure 21. Along the space axis, $x = 2$ represents the first solid layer and $x = j$ the last layer and $x = 1$ and $x = j + 1$ are dummy points on either end. The time axis uses n as a counter. The concentration, C, at any point can be denoted by a space-time subscript e.g., $C_{i+1,n}$ is the concentration at $x = i + 1$ at time n. All the finite differences are written about the point x_i, $t_{n+\frac{1}{2}}$ which is halfway between the known and the unknown time levels. This point is shown as a + in Figure 21. Values of the dependent variable, C, are compared only at the points designated by circles. The finite differences for all the space points at a known time n make up a tri-diagonal matrix. The algorithm used to solve this matrix is a special adaptation of Gaussian Elimination procedure[44] and uses the Neu-

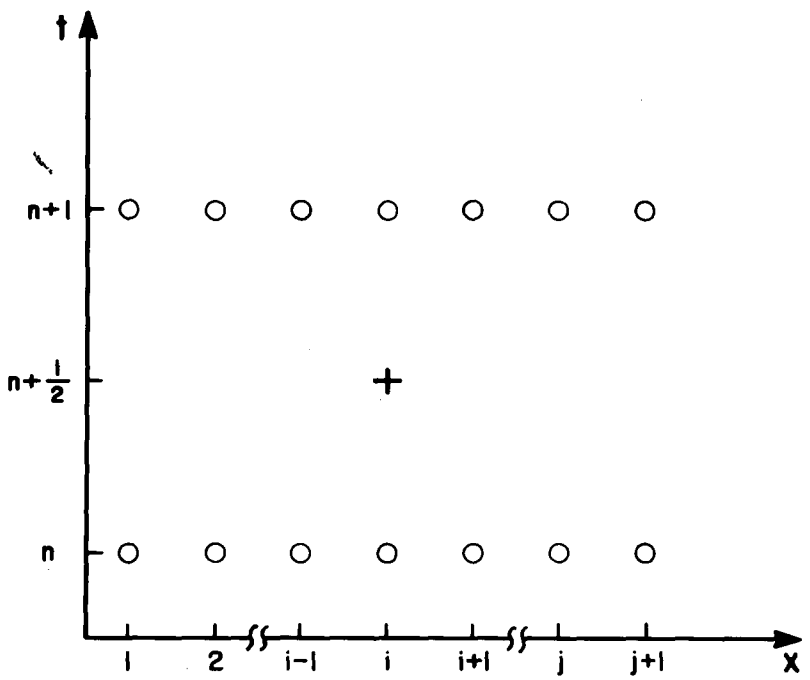

Fig. 21 - A space-time grid for diffusion calculation.

mann boundary conditions. The boundary conditions are satisfied by setting $C_{1,n} = C_{3,n}$ and $C_{j+1,n} = C_{j-1,n}$. This is equivalent to setting the concentration gradient equal to zero at both ends. Appendix I shows a listing of the computer program.

RESULTS

This section contains the results of the directional solidification experiments, the diffusion couple experiments and the equilibrium partition coefficient experiments.

A. Critical Growth Rate Estimate

The directional solidification experiments were done with binary Fe-Ni alloys containing about 10% nickel. Growth rates ranging from 0.8×10^{-3} cm/sec to 3×10^{-3} cm/sec were investigated. The growth morphologies for the different growth rate experiments are listed in Table 6. The results indicate that the plane front growth breaks down to cellular growth somewhere between 1.6×10^{-3} cm/sec and 1.8×10^{-3} cm/sec. Figure 8 shows a planar front growth at 1.6×10^{-3} cm/sec and Figure 9 shows a cellular growth at 1.8×10^{-3} cm/sec. An average growth rate of 1.7×10^{-3} cm/sec was chosen as the critical growth rate. This critical growth combined with a thermal gradient of 100°K/cm in the liquid yields a critical G/R ratio of about $60{,}000^{\circ}$K sec/cm^2 (see equation 3). This G/R value implies that for Fe-Ni alloys containing $\sim$ 10% Ni, a planar growth front would break down for G/R ratios less than $60{,}000^{\circ}$K sec/cm^2. Based on these results a growth rate of about 3×10^{-3} cm/sec was chosen for the cellular dendritic solidification experiments.

B. Partition Coefficients From Dendritically Solidified Alloys

The microprobe data from the transverse sections of the

Sample #	Growth Rate (cm/sec)	Growth Morphology
A0	0.83×10^{-3}	Plane front
A1	1.60×10^{-3}	Plane front
A2	1.79×10^{-3}	Cellular
A3	2.12×10^{-3}	Cellular
A4	2.78×10^{-3}	Cellular

Table 6 - Growth morphologies for different growth rates.

dendritically solidified alloys are listed in Table 7. Figure 11 shows a typical transverse section that was used for both core and bulk analyses. Table 7 lists the core and bulk compositions of the alloys prepared. The ratio of the core composition to the bulk composition is listed under K_D^X and is the measured partition coefficient. It should be noted that K_D^X values for Ni, P, Ge, Au and Ce are less than unity while K_D^X for Pt and Ir are greater than one. The errors associated with the analyses are also listed in Table 7 and will be discussed later.

C. Determination of Diffusion Coefficients

For a ternary or a higher order system the diffusion behaviour can be described by Onsager's extension of Fick's law. For a ternary system, like Fe-Ni-Ge for example, when diffusivities are assumed to be composition independent, Fick's second law can be written as

$$\frac{dC_{Ni}}{dt} = D_{NiNi} \frac{\partial^2 C_{Ni}}{\partial X^2} + D_{NiGe} \frac{\partial^2 C_{Ge}}{\partial X^2} \qquad 8a$$

$$\frac{dC_{Ge}}{dt} = D_{GeNi} \frac{\partial^2 C_{Ni}}{\partial X^2} + D_{GeGe} \frac{\partial^2 C_{Ge}}{\partial X^2} \qquad 8b$$

where D_{NiNi} and D_{GeGe} are the major coefficients. The major coefficients are measures of the influences of the concentration

Alloy #	Ternary Element, X	Nickel Content wt%	Bulk Composition wt% X	Composition of Dendrite Cores	Partition Coefficient K_D^X (Measured)
A12t	'*'	11.18	11.18 ± 0.25 Ni	9.8 ± 0.1	0.88 ± 0.02
A13t	Platinum	10.67	1.27 ± 0.01	1.72 ± 0.1	1.35 ± 0.08
A15t	Phosphorus	12.25	0.55 ± 0.03	0.23 ± 0.01	0.42 ± 0.03
A16t	Germanium	11.17	0.86 ± 0.02	0.59 ± 0.01	0.69 ± 0.02
A17t	Gold	11.2	0.58 ± 0.06	0.27 ± 0.01	0.47 ± 0.05
A19t	Cerium	9.52	1.68 ± 0.04	0.23 ± 0.02	0.14 ± 0.01
A18	Iridium	9.88	1.00 ± 0.20	1.73 ± 0.01	1.73 ± 0.3

'*' Sample A12t is a binary Fe-Ni Alloy

Table 7 - Core and bulk compositions of the directionally solidified alloys.

gradients of the elements on their own fluxes. The terms D_{NiGe} and D_{GeNi} are the cross-coefficients and are measures of the influence of the gradient of one element on the flux of the other. In the diffusion experiments carried out in this study the Ni concentrations on either side of the couple were nearly the same ($\sim$ 10%) and the ternary additions were small ($\sim$ 1%). The effects of cross-coefficients were observed to be very small. The Matano analysis yields the major coefficient of the ternary element. The results of the Matano analysis are given in Table 8. The diffusivities refer to the major coefficient D_{XX} of the element X in Fe-10% Ni-0.5% X alloys. For both gold and germanium an Arhhenius type relationship was assumed between the diffusivities and absolute temperature. The diffusivity can be expressed as

$$D = D_o \exp [-Q/RT] \qquad 9$$

where D_o is the frequency factor, Q is the activation energy, R is the gas constant and T the temperature in ^oK. For a plot of ℓnD vs 1/T, Q is the slope of the straight line and $\ell n\, D_o$ is the intercept at 1/T = 0. The Arhhenius plot for gold is shown in Figure 22 where a least squares straight line is drawn through the data points. A similar plot for germanium is shown in Figure 23. The D_o and Q values estimated are as follows:

For gold:

$$D_o = 1.71 \times 10^{-4} \text{ cm}^2/\text{sec}$$

$$Q = 43280 \text{ cal.}$$

Element	Diffusion Temperature °K	Diffusion Time (sec)	$\tilde{D}$ The Major Coefficient of X in Fe-10%Ni-0.5%X
Gold	1363	22.68×10^{4}	1.96×10^{-11}
Gold	1433	9.18×10^{4}	4.49×10^{-11}
Gold	1468	9.45×10^{4}	6.21×10^{-11}
Germanium	1253	22.50×10^{4}	9.12×10^{-12}
Germanium	1358	12.96×10^{4}	4.21×10^{-11}
Germanium	1493	5.76×10^{4}	4.90×10^{-10}

Table 8 - Diffusivities from Matano Analyses.

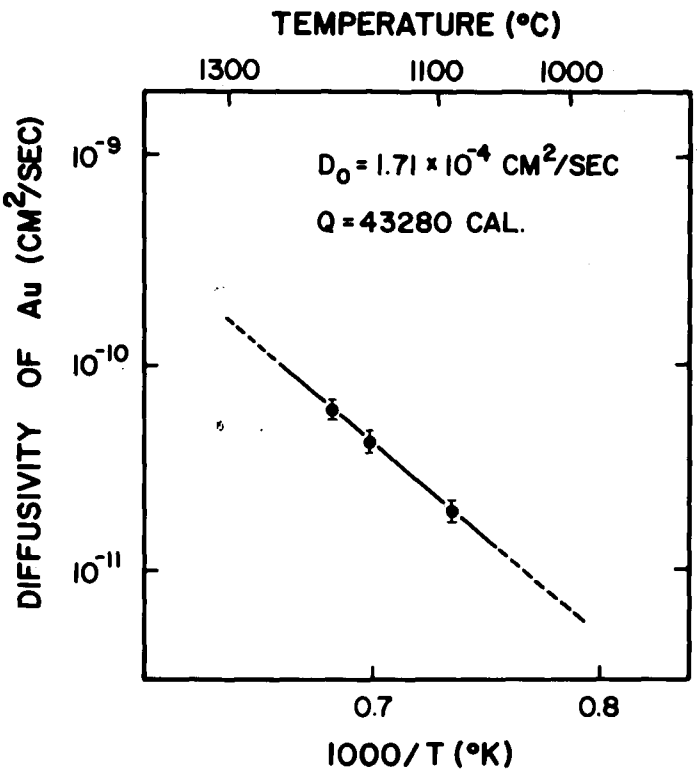

Fig. 22 - Temperature dependence of the major diffusion coefficient of Au in γ Fe-Ni.

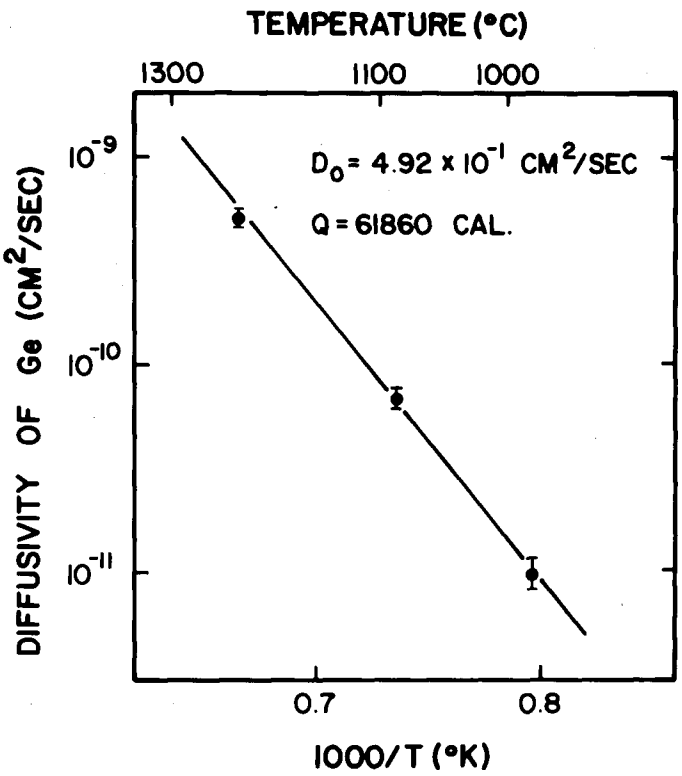

Fig. 23 - Temperature dependence of the major diffusion coefficient of Ge in γ Fe-Ni.

For germanium:

$$D_o = 4.92 \times 10^{-1} \text{ cm}^2/\text{sec}$$

$$Q = 61860 \text{ cal.}$$

In both cases the Matano analysis did not show any systematic variation of diffusivity with composition.

For the other elements the diffusivities were taken from literature.

i) For nickel, the diffusivity in γ Fe, as reported by Goldstein et al.[47] is

$$D_\gamma = \exp [1.15 + 0.0519\ C_{Ni}(wt\%)] * \exp [-(76400 - 11.6\ C_{Ni}(wt\%))/RT] \text{ cm}^2/\text{sec} \quad 10$$

where C_{Ni} is the concentration of nickel, R is the gas constant and T is the temperature in ^oK.

ii) The diffusivity for P in γFe-Ni was taken from the data reported by Heyward and Goldstein.[48] The major coefficient for P is expressed as

$$D_P = 9 \times 10^{-2} * \exp [-50200/RT] \text{ cm}^2/\text{sec} \quad 11$$

iii) The diffusion coefficient for Pt was taken from the work done by Kucera and Million[49] on self-diffusion of Pt in Fe-Pt alloys. In the temperature range 780-1420^{o}C the self diffusion coefficient of Pt in Fe-0% Pt alloy is given as

$$D_{Pt} = 2.7 * \exp [-70700/RT] \text{ cm}^2/\text{sec} \quad 12$$

iv) The diffusivity of Ir in Fe or Fe-base alloys is not documented in the literature. Ir has a f.c.c. structure like Ni and has a melting point

1000^{o}K above that of Ni. The diffusivity of Ir need only be considered if the diffusion effects on nickel are important.

D. Solid State Diffusion Effects

Partition coefficients K_D^X were measured from cellular growth experiments as described earlier in Section D of experimental technique. These K_D^X values were corrected for solid state diffusion effects. The measured partition coefficients K_D^X and the calculated equilibrium partition coefficients are listed in Table 9. The diffusivities of the elements at 1300^{o}C are also listed in the table. The measured and corrected K_D^X values indicate that diffusion effects become important if the element has a diffusivity greater than 1×10^{-10} cm^2/sec at 1300^{o}C. Figure 24 shows the effect of solid state diffusion on the segregation of nickel. The dendrite core composition is barely altered. Figure 25 shows the effect of diffusion on the segregation profile of Ge. The core composition, in this case, is noticeably altered due to the higher diffusivity of Ge. It was pointed out in the previous subsection that Ir has a much lower diffusivity than nickel. Since the diffusion effects for Ni are minimal, the diffusion effects for Ir have been ignored.

The effect of diffusion can be divided into two parts. The first is diffusion during solidification and the second is diffusion after solidification during subsequent cooling to 1000^{o}C. Elements like Ge and Au when added up to 1% by weight, in Fe-10%

Third Element, X	K_D^X Measured	K_D^X Equilibrium	Diffusivity at 1300°C cm^2/sec
Ge	0.69	0.58	1.25×10^{-9}
Au	0.47	0.43	1.66×10^{-10}
Pt	1.35	1.45	4.05×10^{-10}
P	0.42	0.12	9.53×10^{-9}
Ce	0.14	--	---
Ni	0.88	0.87	1.33×10^{-10}
Ir	1.73	1.73	---

Table 9 - Measured and corrected K_D^X values.

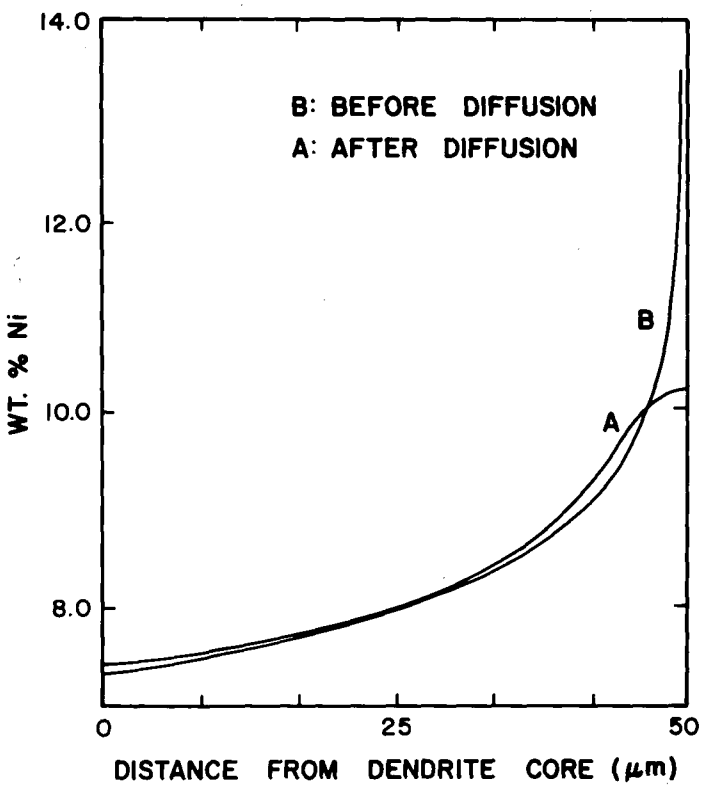

Fig. 24 - Ni profiles before and after diffusion.

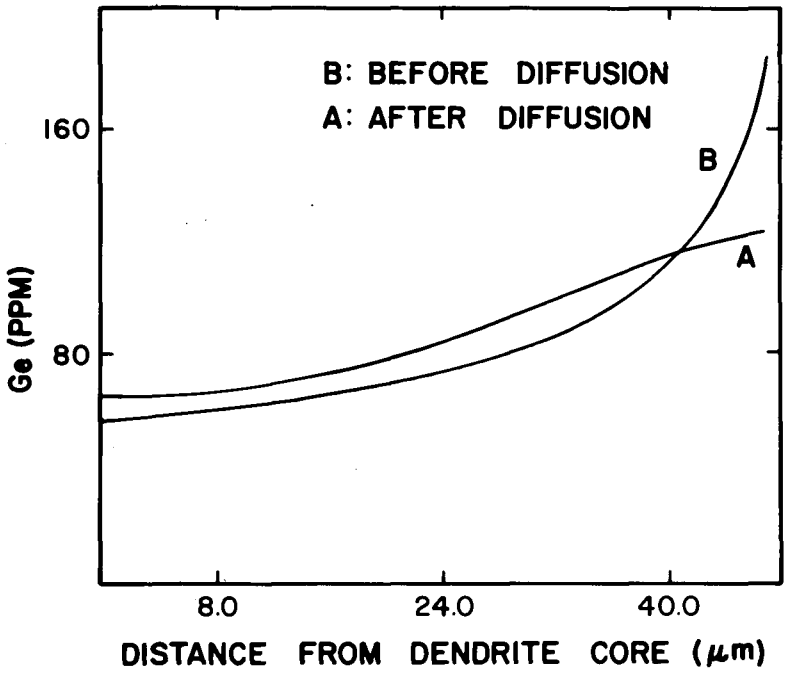

Fig. 25 - Ge profiles before and after diffusion.

Ni alloys, make diffusion insignificant in the solidification range. These Fe-Ni-X ternary alloys have a freezing range of $\sim 5^{o}C$. In such cases the diffusion during solidification is negligible compared to the diffusion during subsequent cooling. On the other hand, elements like P and S substantially alter the solidification range of Fe-Ni alloys. Figure 26 shows a pseudo-binary Fe-9% Ni phase diagram. The data points are taken from the equilibrium partition coefficient experiments. The solidification range increases by $\sim 100^{o}C$ for every 0.25% P, till the eutectic isotherm is reached. The equilibrium experiments use Fe-Ni-P-Ge alloys containing $\leq$ 1% Ge. The effect of Ge on the Fe-Ni-P system is ignored. Experiments with and without Ge yielded similar P levels in the solid and liquid phases. This indicates that the effect of Ge, on the Fe-P pseudo-binary, is masked by the experimental errors. Because of the greatly expanded solidification range in Fe-Ni-P alloys, the diffusion during solidification becomes as important as diffusion after solidification. An alloy with 1.25% P has a solidification range of almost $500^{o}C$. In this case, the temperature at the end of the freezing process is almost $1000^{o}C$. The diffusion after solidification is therefore negligible compared to diffusion during solidification. Figure 27 shows an example of an Fe-Ni-P alloy where both stages of diffusion play an important role. The curve 'I' denotes an intermediate stage when solidification is just complete. This profile is further modified by diffusion after solidification as indicated by curve 'A.'

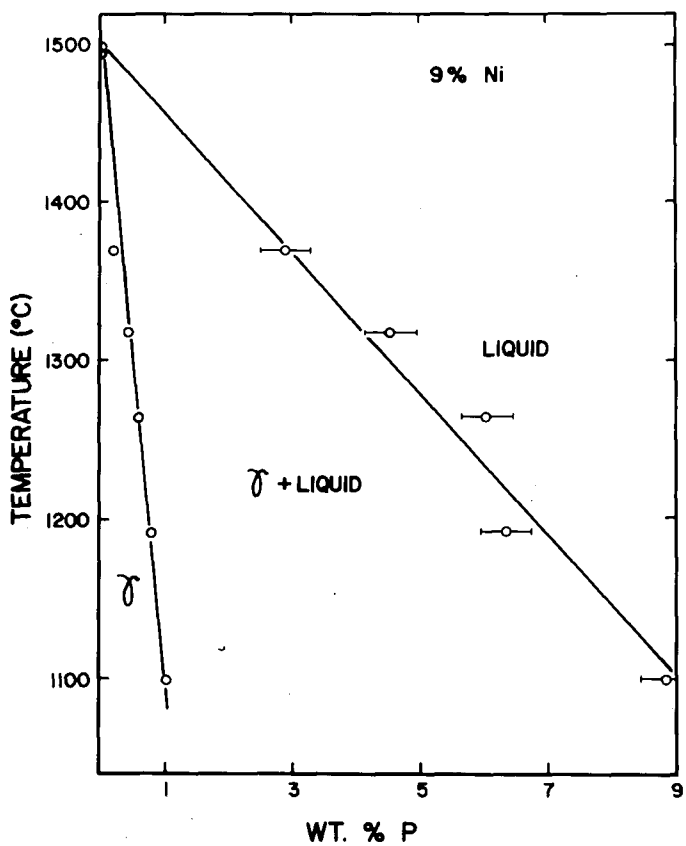

Fig. 26 - An Fe-P pseudo-binary phase diagram.

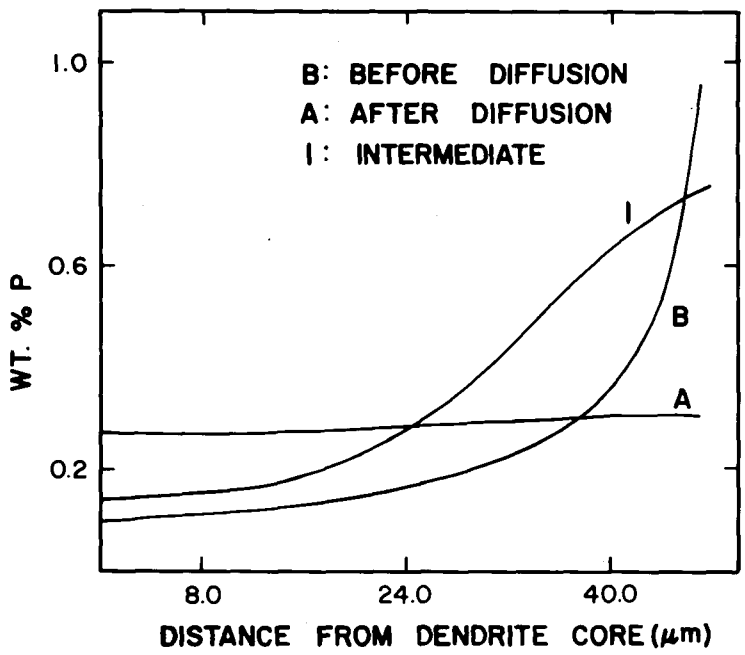

Fig. 27 - Phosphorus profiles before, during and after diffusion.

E. Equilibrium Partition Coefficients

Quantitative data from the equilibrium partition coefficient experiments are presented in this section. To confirm that equilibrium was attained in the samples, composition of the grains were measured randomly over the cross sections of the samples. Grains from different regions had similar compositions. In addition, composition traces were taken across some grains to look for signs of zonation. No evidence of compositional inhomogeneity was found. Results from both techniques confirmed that equilibrium was attained. Figure 28 shows a typical grain that was chosen for a composition trace. The arrow points to the contamination spots from the microprobe analysis. Figure 29 shows the compositional homogeneity of that grain. A small increase in the P concentration near the edge of the grain is associated with solidification during the quench. Quantitative analysis of the dendritically solidified liquid presented some problems. The choice of a representative pool of liquid was important. Area scans and defocussed beam analysis were used as described earlier. Narrow strips of liquid that had solidified between solid grains were avoided because the finite growth of the grains during the quench results in the rejection of P into the liquid ($K_D^P < 1$, see Table 7). If the amount of liquid, trapped between the grains, is small then its composition is noticeably increased. Figure 30 shows an example where a small strip of liquid has reached the eutectic composition. Small pools of liquid were avoided for the same reason. Figure 19

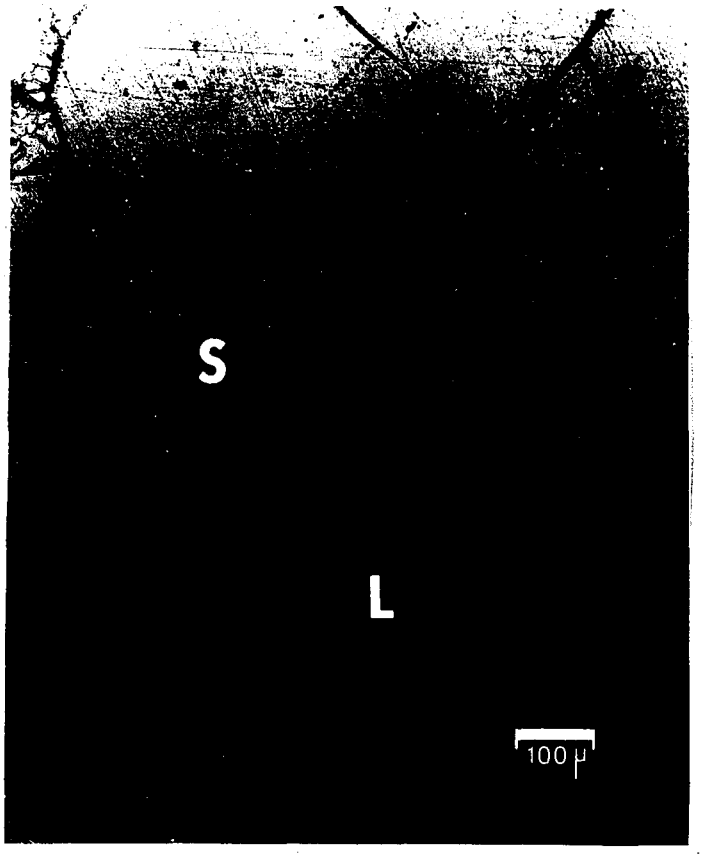

Fig. 28 - A typical probe trace to check for equilibrium.

S: solid
L: modified liquid
Arrow: points out the trace.

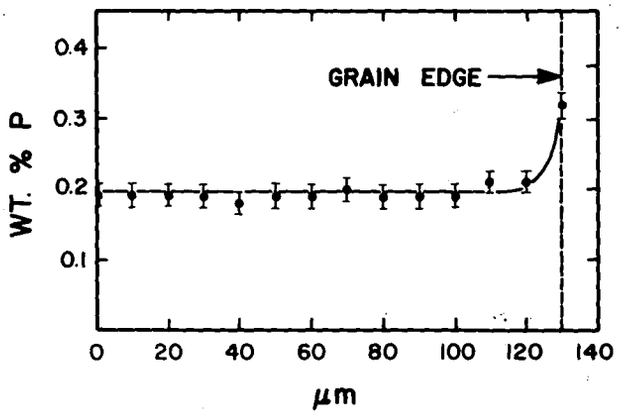

Fig. 29: Compositional homogeneity in the solid phase.

Fig. 30 - A small strip of liquid raised to the eutectic composition.

shows pools of liquid that were large enough to be compositionally invariant during the quench. Table 10 shows the data obtained from many solid and liquid analyses for a sample held at 1099°C for 3.0 hours. The small spread in the composition data from the solid indicates equilibrium has been obtained. The greater spread in the composition data from the liquid is partially due to the selection of pools of liquid of different sizes. Even within a pool of liquid a small range of compositions can be expected due to the sampling differences during area scans or defocussed beam analyses.

Table 11 gives the K_D^{Ge} values for different temperatures and phosphorous levels in the solid. Figure 31 shows this dependence. Notice the sharp increase of K_D^{Ge} for small increases in the P level in the solid. A least squares line drawn through the data points yields the following functional dependence:

$$K_D^{Ge} = C_P * 1.06 + 0.54 \qquad 13$$

where C_P is the P concentration of the solid. Correlating K_D^{Ge} with the temperature of the experiment yields a relationship

$$K_D^{Ge} = -2.83 \times 10^{-3} T + 4.73 \qquad 14$$

where T is the temperature in degrees Celsius. The errors listed in the tables will be discussed in a later section.

A preliminary experiment was performed using an Fe-Ni-Ge-S alloy containing ~ 0.5% Ge and 2-3% sulfur. The alloy was equilibrated at 1292°C for 2 hours. Subsequent microprobe

# of analysis	%Ni (wt) in solid	%Ni (wt) in liquid	%P (wt) in solid	%P (wt) in liquid	%Ge (wt) in solid	%Ge (wt) in liquid
1	8.37	9.85	1.01	8.04	1.07	0.79
2	8.25	10.01	1.02	8.28	1.03	0.73
3	8.21	9.85	1.01	9.42	1.09	0.67
4	8.61	10.33	1.01	8.82	1.08	0.66
5	8.46	10.18	1.02	8.79	1.05	0.64
6	8.34	9.59	1.02	9.05	1.09	0.63
7	8.47	9.97	1.02	9.16	1.09	0.62
8	8.26	9.56	1.00	8.81	1.03	0.66
9	8.09	10.02	1.02	8.54	1.04	0.65
10	8.16	9.76	1.02	9.10	1.08	0.65
11	8.08	9.82	1.01	10.39	1.08	0.54
12	8.38	9.50	1.02	8.72	1.11	0.72
13	8.20	9.94	1.02	8.27	1.21	0.73
14	7.90	9.35	1.02	8.89	1.14	0.67
15	7.80	10.14	0.99	9.11	1.04	0.68
Average	8.24	9.86	1.015	8.89	1.08	0.67
	$\pm$0.19	$\pm$0.23	$\pm$0.004	$\pm$0.41	$\pm$0.04	$\pm$0.05
	$K_D^{Ni} = 0.84 \pm 0.03$		$K_D^{P} = 0.114 \pm 0.005$		$K_D^{Ge} = 1.61 \pm 0.14$	

Table 10 - Typical data obtained from an equilibrium experiment.

Sample #	T(°C)	P (wt%) in solid	Ge (wt%) in solid	Ge (wt%) in liquid	K_D^{Ge}
E11	1099°C	1.02 ± 0.004	1.08 ± 0.04	0.67 ± 0.05	1.61 ± 0.14
E5	1192°C	0.79 ± 0.02	1.14 ± 0.02	0.82 ± 0.04	1.39 ± 0.07
E4	1265°C	0.62 ± 0.01	1.10 ± 0.04	0.89 ± 0.04	1.24 ± 0.07
E10	1318°C	0.43 ± 0.02	0.78 ± 0.03	0.81 ± 0.04	0.96 ± 0.06
E8	1370°C	0.20 ± 0.006	0.82 ± 0.01	1.15 ± 0.03	0.71 ± 0.02
A16t	1500°C	0.00	---	---	0.58(*)

*This data point is taken from a dendritically solidified ternary alloy Fe-Ni-Ge.

Table 11 - Dependence of K_D^{Ge} on the phosphorus content and the temperature.

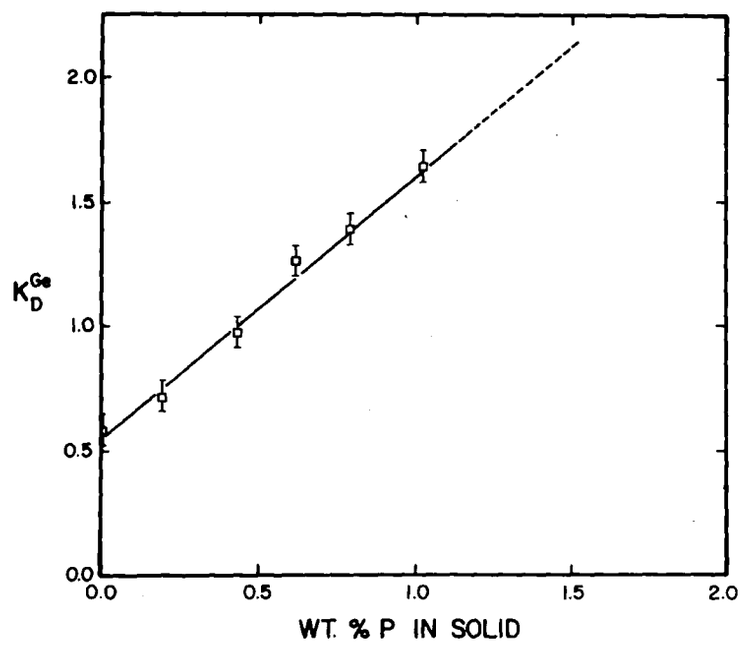

Fig. 31 - Functional dependence of K_D^{Ge} on the P content in the solid.

analysis did not show any measurable Ge in the liquid (< 0.01 wt%) while indicating 0.47 wt% Ge in the solid. Assuming arbitrarily that the microprobe would not detect Ge below 0.01 wt%, K_D^{Ge} is greater than or equal to 0.47/0.01, i.e., $K_D^{Ge} \geq 47$.

DISCUSSION

A. Quality of Data

This subsection discusses the quality of the results presented in the previous section. The sources of errors and error estimations for the experiments are discussed.

A.1. Errors in critical growth rate determination

The growth rate (R) of the solid-liquid interface was calculated by measuring the distance traversed by the crucible in a fixed period of time. Assuming that the motor runs at a constant speed during an experiment, the maximum error associated with the estimation of distance is 1 mm in 15 mm, i.e., 7 relative %. The critical growth rate was between the limits 1.6×10^{-3} cm/sec and 1.8×10^{-3} cm/sec (see Table 6). An error bar of 7 relative percent drawn around an average value of 1.7×10^{-3} cm/sec includes both the limits. The average is therefore a good estimate of the critical growth rate. The thermal gradient (G) in the liquid was evaluated using equation 3. The slope of the liquidus line, on the Fe-Ni phase diagram, was estimated with a least squares line drawn through the data points generated by Hellawell and Hume-Rothery.[40] An error of $\sim 5\%$ relative can be associated with it. K_D^{Ni} was taken as 0.88 and has an error of ± 0.01. The diffusivity in the liquid, D_L, was taken as 4.5×10^{-5} cm^2/sec. This term is the biggest source of error and overrides all other errors. A recent study[50] has indicated that D_L decreases as the interface is approached. A maximum error

of 10% was assumed for the critical G/R ratio. This makes the critical G/R ratio 60,000 $\pm$ 6,000^{o}K sec/cm^{2}.

A.2. Errors in the measured K_D^X values

Table 7 gives the dendrite core compositions, the bulk compositions and the estimates of K_D^X values. The errors associated with the measurements are discussed below. In all cases 15 to 20 point analyses were taken on the cell centers to measure the core composition. The maximum/minimum composition, as the case may be, was taken as the core composition. The error in this core composition measurement arises from the statistical nature of the x-ray emission phenomenon. The error will depend on the total number of x-ray counts accumulated at that point.[38] The relative error would be $\pm$ $(3/\sqrt{N})$ * 100%, where N is the total x-ray counts gather at that point. In the case of bulk composition estimation, the average of all the area scans was taken. The standard deviation associated with the average value is given by[38]

$$S_C = \left[\sum_{i=1}^{n} (N_i - \bar{N}_i)^2/(n-1) \right]^{\frac{1}{2}} \qquad 15$$

where Ni is the number of counts for each analysis, i, and

$$\bar{N}_i = \sum_{i=1}^{n} N_i/n$$

where n is the number of determinations of i. The error in the average value for the bulk composition is $\pm$ $(S_C/\bar{N}_i)$ * 100 relative percent. The measured partition coefficient K_D^X is the ratio of

the core composition to the bulk composition (see equation 2) and is therefore accompanied by a compounded error. If E_1 is the error in the numerator and E_2 that in the denominator, both in relative percent, the error in the estimation of K_D^X is $(E_1^2 + E_2^2)^{\frac{1}{2}}$ relative percent.

A.3. Quality of diffusivity data

The diffusivity for Au and Ge were calculated using the Matano Analysis. The graphical integrations were performed on 55 cm x 45 cm graph sheets. The two sources of error are the estimation of area and the calculation of the slope (see equation 5). The error in counting the area is about 3 relative % while that in measuring the slope is about 6 relative %. Since the diffusion times were long (between 16 hrs. and 64 hrs.) an error of about 5 minutes in estimating the diffusion time was ignored. Compounding these errors, a maximum of 10% relative was assigned to the diffusivity numbers. The maximum error in measuring the temperature is $5^{\circ}C$ and since the experiments were conducted around $1000^{\circ}C$ the errors are less than 0.5% relative.

Diffusion coefficients are normally estimated over a wide range of temperatures. In this study, diffusion coefficients below $1000^{\circ}C$ were not required. Therefore the experiments were done only in the range $1300^{\circ}C$ to $1000^{\circ}C$. Least squares lines were drawn through the data points recorded in this range. Any errors in the slopes and intercepts that result from drawing least squares lines show up as errors in D_o and Q values. The estimated errors are:

i) For Au: $D_o = 1.74 \times 10^{-4} \pm 1 \times 10^{-4}$ cm^2/sec

$Q = 43280 \pm 3000$ cal.

ii) For Ge: $D_o = 0.492 \pm 0.2$ cm^2/sec

$Q = 61856 \pm 2000$ cal.

A.4. Error analysis for the equilibrium partition coefficient measurements

The quantitative microprobe analysis for the equilibrium experiments required two kinds of measurements. One was random point analyses on several grains and the other a series of area scans or defocussed beam analyses on the modified liquid phase. In both cases at least 15 data points were collected. The error analysis involved calculating the range of homogeneity (see equation 4) for Ni, P and Ge in both liquid and the solid. Tables 12 through 16 show the homogeneity data for the different alloys equilibrated at different temperatures. In all cases a 99% confidence level was chosen. The equilibrium partition coefficient K_D^X is the ratio of the concentration of X in the solid to that in the liquid (see equation2). If $\pm R_S$ is the range of compositions in the solid and $\pm R_L$ the range in the liquid, both in relative percent, then the range of K_D^X values is $\pm (R_S^2 + R_L^2)^{\frac{1}{2}}$, also in relative percent.

B. Trace Element Fractionation within Groups

The grouping of iron meteorites on a log X vs log Ni plot was discussed at length in the Background Section. The implications of Scott's plane front solidification theory were reviewed.

Element	n	$t_{n-1}^{1-\alpha}$	$S_c/\bar{N}$	$C \pm W$	K_D^X
Nickel in Solid	15	2.977	0.02	9.19 ± 0.14	0.89 ± 0.02
Nickel in Liquid	16	2.947	0.02	10.29 ± 0.15	
Phosphorus in Solid	15	2.977	0.02	0.62 ± 0.02	0.1 ± 0.003
Phosphorus in Liquid	16	2.947	0.07	6.06 ± 0.07	
Germanium in Solid	15	2.977	0.05	1.10 ± 0.05	1.24 ± 0.1
Germanium in Liquid	16	2.947	0.06	0.89 ± 0.06	

Confidence Level - 99%
Equilibration Temperature - 1262°C

Table 12 - Level of Homogeneity for Sample E-4.

Element	n	$t_{n-1}^{1-\alpha}$	$S_c/\overline{N}$	$C \pm W$	K_D^X
Nickel in Solid	18	2.898	0.020	9.37 ± 0.13	0.9 ± 0.01
Nickel in Liquid	15	2.977	0.016	10.40 ± 0.09	
Phosphorus in Solid	18	2.898	0.040	0.79 ± 0.02	0.12 ± 0.01
Phosphorus in Liquid	15	2.977	0.070	6.35 ± 0.34	
Germanium in Solid	18	2.898	0.030	1.14 ± 0.02	1.39 ± 0.07
Germanium in Liquid	15	2.977	0.060	0.82 ± 0.04	

Confidence Level - 99%
Equilibration Temperature - $1192^{o}C$

Table 13 - Level of Homogeneity for Sample E-5.

Element	n	$t^{1-\alpha}_{n-1}$	$S_c/\overline{N}$	$C \pm W$	K_D^X
Nickel in Solid	19	2.878	0.016	13.10 ± 0.14	0.86 ± 0.02
Nickel in Liquid	18	2.898	0.031	15.32 ± 0.32	
Phosphorus in Solid	19	2.878	0.051	0.20 ± 0.006	0.07 ± 0.01
Phosphorus in Liquid	18	2.898	0.130	2.91 ± 0.26	
Germanium in Solid	19	2.878	0.020	0.82 ± 0.01	0.71 ± 0.02
Germanium in Liquid	18	2.898	0.035	1.15 ± 0.03	

Confidence Level - 99%
Equilibration Temperature - 1370°C

Table 14 - Level of Homogeneity for Sample E-8.

Element	n	$t^{1-\alpha}_{n-1}$	$S_c/\bar{N}$	$C \pm W$	K_D^X
Nickel in Solid	14	3.012	0.025	8.78 ± 0.18	0.87 ± 0.02
Nickel in Liquid	16	2.947	0.013	10.12 ± 0.10	
Phosphorus in Solid	14	3.012	0.070	0.43 ± 0.02	0.09 ± 0.01
Phosphorus in Liquid	16	2.947	0.135	4.53 ± 0.45	
Germanium in Solid	14	3.012	0.040	0.78 ± 0.03	0.96 ± 0.06
Germanium in Liquid	16	2.947	0.070	0.81 ± 0.04	

Confidence Level - 99%
Equilibration Temperature - 1318°C

Table 15 - Level of Homogeneity for Sample E-10.

Element	n	$t^{1-\alpha}_{n-1}$	$S_c/\overline{N}$	$C \pm W$	K_D^X
Nickel in Solid	15	2.977	0.03	8.24 ± 0.19	0.84 ± 0.03
Nickel in Liquid	15	2.977	0.03	9.86 ± 0.23	
Phosphorus in Solid	15	2.977	0.005	1.02 ± 0.004	0.115 ± 0.005
Phosphorus in Liquid	15	2.977	0.06	8.89 ± 0.41	
Germanium in Solid	15	2.977	0.05	1.08 ± 0.04	1.61 ± 0.13
Germanium in Liquid	15	2.977	0.09	0.67 ± 0.05	

Confidence Level - 99%
Equilibration Temperature - 1099°C

Table 16 - Level of Homogeneity for Sample E-11.

Special attention was drawn to the fact that the plane front growth model does not explain the trends seen in a log Ge vs log Ni plot. The model predicts that all the chemical groups would have a constant and similar slope. Group IVA meteorites exhibit a positive decreasing slope. Group I meteorites show a negative slope. Group IIIAB meteorites have a slope going from positive to negative. The three groups mentioned above encompass nearly 70% of all iron meteorites. In view of this inconsistency in the model there is a need for a more refined theory that can explain the changing trends in the different chemical groups. In the following subsections a single solidification and diffusion model will be developed that will explain the Ge-Ni correlations in the iron meteorite chemical groups. The model is based solely on experimental results and computer modeling.

B.1. Solidification mode in meteorites

The critical thermal gradient to growth rate ratio (G/R) that governs the break down of a plane front growth for an Fe-10% Ni alloy was found to be 60000 $\pm$ 6000^{o}K sec/cm^{2}. Computer modeling was used to estimate the G/R ratios in meteorite parent bodies.[51] The model uses parent bodies made up of iron-nickel cores with silicate shells. Calculations of G/R ratios were done for parent bodies ranging from 10 km to 800 km in outer radius (r_o). The ratio of the metallic core radius (r_c) to the parent body radius (r_o) ranged from 0.125 to 0.75. In all cases the maximum G/R ratio did not exceed 3000^{o}K sec/cm^{2}. This maximum G/R ratio is more than one order of magnitude below the G/R ratio

required for a stable plane front growth. Based on these results it is reasonable to expect parent bodies to solidify dendritically.

B.2. Dendrite size in parent bodies

Having ascertained that meteorite parent bodies freeze dendritically, it is required to estimate the size of the dendrites. Flemings et al.[35] have conducted a detailed study on dendrite arm spacing as a function of cooling rate. They have shown that the secondary arm spacing of dendrites varies systematically with the cooling rate. Their experiments included cooling rates ranging over five orders of magnitude. The authors also point out that a similar trend is observed for primary dendrites. Barone et al.[52] have carried out a series of experiments with Fe-Ni alloys and have documented the primary dendrite arm spacings as a function of solidification times. Table 17 shows the primary dendrite spacing (d) and the square root of the solidification time (θ_f) for a range of cooling rates. The ratio of the spacing to the square root of the solidification time is constant to within 10% relative over two orders of magnitude. If d is expressed in microns and θ_f in seconds then the average value of $d/\sqrt{\theta_f}$ is $\sim 26\ \mu m/\sqrt{sec.}$ A reasonable estimate for the cooling rate of meteoritic bodies is $\sim 1^{o}C$ per million years.[53] The solidification range for an Fe-10% Ni alloy is $5^{o}C$. This needs a solidification time of ~ 5 million years. Extension of the average $d/\sqrt{\theta_f}$ value to meteoritic solidification times gives a primary dendrite spacing estimate of ~ 325 meters. In order to get another independent estimate for the primary dendrites in parent bodies, some

Solidification time, θ_f (sec)	$\sqrt{\theta_f}$ ($\sqrt{sec}$)	Primary Dendrite Spacing, d(μm)	$d/\sqrt{\theta_f}$
2.62	1.62	47	29.01
7.56	2.75	75	27.30
23.81	4.88	124	25.40
36.00	6.00	165	27.50
50.41	7.10	194	27.32
86.49	9.30	231	24.80
108.20	10.40	260	25.00
132.30	11.50	268	23.30
158.80	12.60	298	23.70
187.70	13.70	334	24.40

Table 17 - Primary dendrite sizes for different solidification times.

experiments were done in the laboratory. Cell sizes were measured for three different cooling rates using the cellular growth equipment described earlier (see Figure 4). Table 18 gives the results. The ratio $d/\sqrt{\theta_f}$ is observed to be constant to within 10% relative. The extension of this data gives a primary dendrite estimate, in parent bodies, of $\sim$ 740 meters. This estimate is about twice the previous estimate. The difference may be due to the entirely different experimental techniques. Barone et al.[52] have shown that the dendrite spacing is very sensitive to several parameters. Both sets of data, however, indicate that dendrites in parent bodies could be typically 0.5 km in width.

B.3. Diffusion in parent bodies

Cellular freezing in parent bodies will lead to dendritic segregation. As seen earlier, this segregation will set up concentration gradients and hence diffusion will modify this profile. The extent to which solid state diffusion will change a dendritic segregation profile depends on three parameters:

i) Diffusivity of the species.

ii) Diffusion time (t).

iii) Distance from dendrite core to edge (x).

The diffusivity is characteristic of the species and the alloy system and is therefore independent of the dendrite size. The ratio of the dendrite core to edge distance (x) and the square root of the diffusion time (t), called the Boltzman function, can be used to relate diffusion in bodies of different sizes. Table 19 compares the Boltzman functions for the dendrites investigated

Sample #	Growth Rate cm/hr.	Dendrite Size, d(μm)	Solidification time, θ (sec)	$d/\sqrt{\theta}$ (cm/$\sqrt{\text{sec}}$)
A2	6.43	150	6.99	57×10^{-4}
A12	12.8	104	3.52	55×10^{-4}
A14	46.5	63	0.97	64×10^{-4}

Average $d/\sqrt{\theta} \approx 59 \times 10^{-4}$ cm/$\sqrt{\text{sec}}$

Table 18 - Cell sizes for different growth rates.

	Experimental Alloys	Estimations in Parent Bodies
x (cm)	50.0×10^{-4}	2.5×10^{4}
t (sec)	5.0×10^{2}	1.58×10^{16}
$x/\sqrt{t}$	2.2×10^{-4}	1.99×10^{-4}

Table 19 - Comparison of Boltzman Functions.

in the laboratory and the dendrites predicted to have formed in parent bodies. The time to cool from 1500°C to 1000°C is taken as the diffusion time, t. A cooling rate of 1°C per million years is assumed for the parent bodies.[53] The similar $x/\sqrt{t}$ values for the two cases indicate that the diffusion effects described earlier for the laboratory dendrites can be extended to meteorite parent bodies with reasonable accuracy. In other words, even though the parent body dendrites are ~0.5 km across the extremely slow cooling rates make solid state diffusion appreciable.

B.4. Fractionation within groups

It was pointed out earlier that a primary fractionation mechanism is believed to be responsible for the formation of meteorite parent bodies. During the early stages of formation these bodies have Fe-Ni cores of uniform compositions corresponding to the average compositions of the meteorite chemical groups. Subsequent cooling leads to dendritic solidification of the molten Fe-Ni cores. Such a cellular freezing results in dendritic segregation as seen earlier. During a later stage these segregated asteroids are broken up by collisions. Since the dendrites in these bodies are ~0.5 km wide, fragments would come from different parts of a dendrite. Figure 32 is a schematic representation of the model. It shows how the meteorites from a chemical group are portions of a dendrite.

B.5. Simulation of chemical groups

A numerical plate model, developed earlier, calculates the segregation profile of an element across a dendrite. Using the

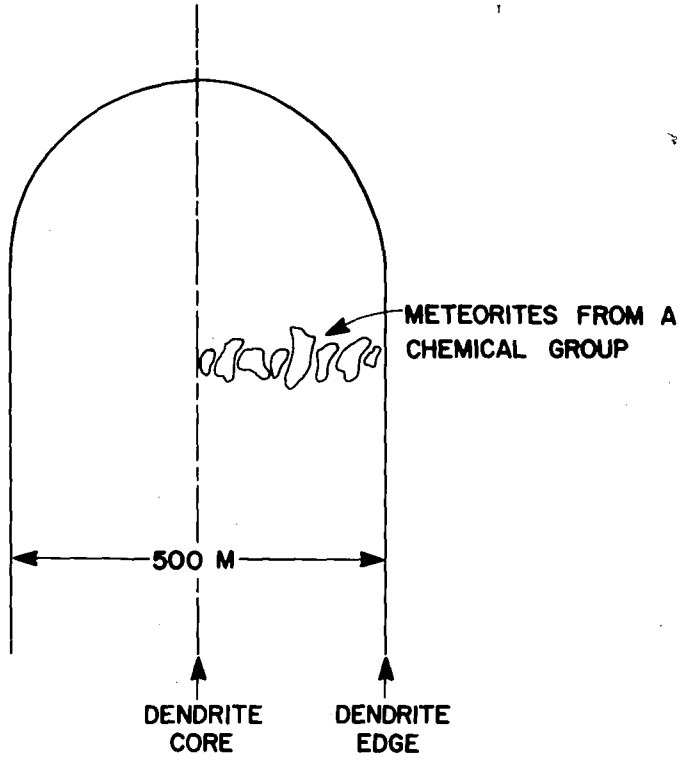

Fig. 32 - A dendrite showing a possible fragmentation pattern.

model for a ternary Fe-Ni-X alloy, the segregation profile of X and Ni, across the dendrite, can be calculated. The two profiles can be combined on a log X vs log Ni plot where each point corresponds to a fixed distance from the dendrite core. Each point on this log-log plot can represent a meteorite. The log-log plot itself can be compared to the log X vs log Ni plots used to study the trends in meteorite groups. The shape of the simulated log X vs log Ni plot will depend on the following factors:

i) Equilibrium partition coefficient of X, K_D^X.

ii) Equilibrium partition coefficient of Ni, K_D^{Ni}.

iii) Diffusion coefficient of X.

iv) Diffusion coefficient of Ni.

v) Starting bulk composition.

Figure 33 shows a group IVA simulation. The (+) sign indicates the starting bulk composition. The profile before diffusion is essentially a straight line, similar to the plane front model. However diffusion modifies this linear relationship. The resultant profile has a curved shape which exhibits a positive decreasing slope. The group IVA meteorites seen in Figure 1 also show a similar nonlinear shape.

A variable K_D^X or K_D^{Ni} can have a significant effect on the shape of the simulated log X vs log Ni plot. Figure 34 shows a log P vs log Ni plot for group IVA and group IIIAB meteorites.[54] It is worth noting that the P levels in group IIIAB is a continuum, with group IIIB having more P than group IIIA. The log Ge vs log Ni plot in Figure 1 shows group IIIB having a negative slope

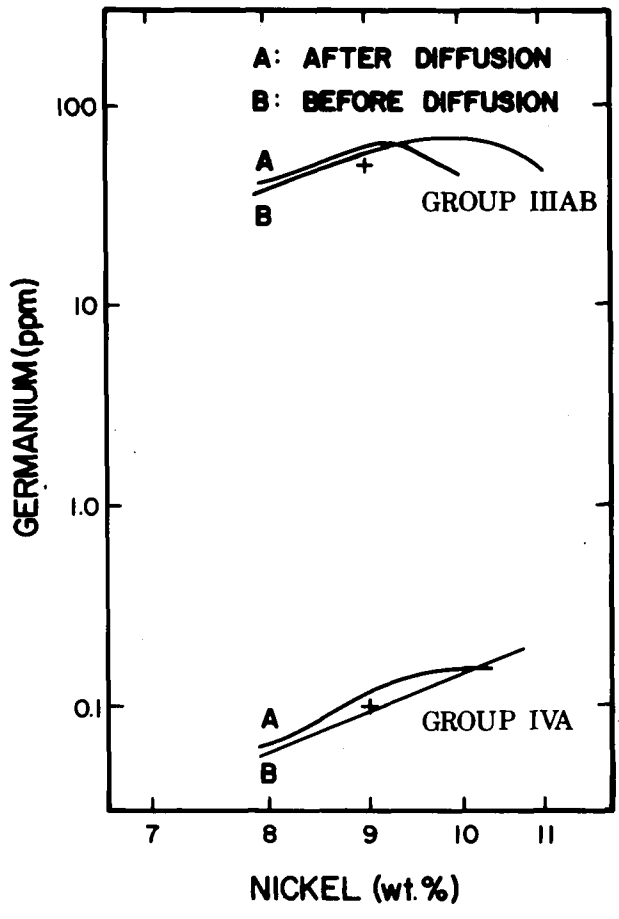

Fig. 33 - Simulation of the shapes of groups IVA and IIIAB.

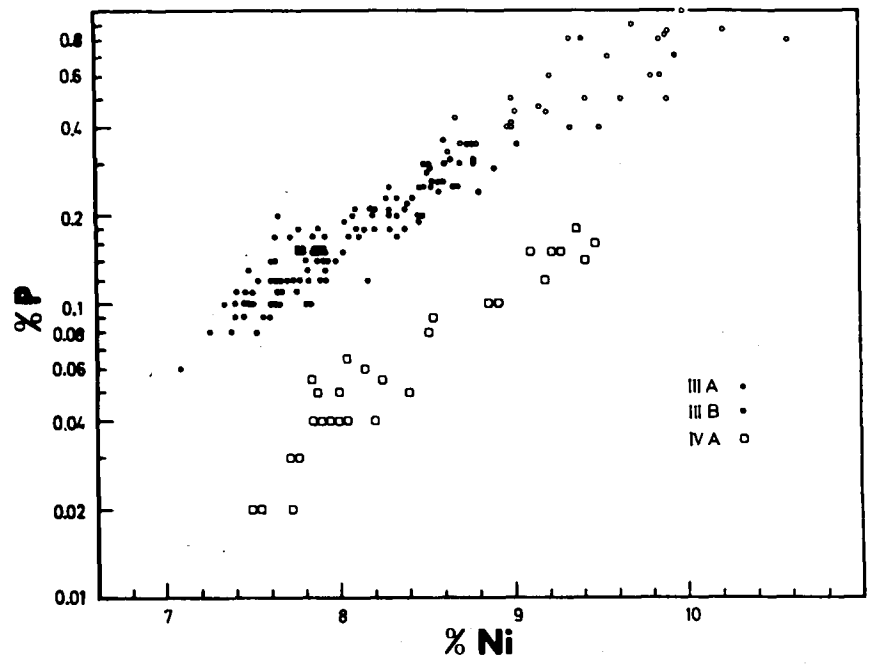

Fig. 34. A log P vs. log Ni plot for the meteorite chemical groups IIIAB and IVA.

and group IIIA a positive slope. It was pointed out earlier in Section D of results that P has a significant influence on the solidification range of Fe-Ni alloys. The solidification range increases by as much as 100°C for every 0.25% P added to the Fe-Ni alloy (see Figure 26).

In addition to widening the freezing range of Fe-Ni-Ge alloys, P also has a drastic effect on the partitioning behaviour of Ge. Figure 31 shows K_D^{Ge} increasing sharply from 0.58 to more than 1 for just 0.5% P in the solid. This dependence (see equation 13) was used in the model to generate the Ge profile. A bulk Ge and Ni content similar to the average composition of group IIIAB was chosen. A phosphorous level of 0.75% was used. Figure 33 shows the simulation of group IIIAB. The increase in K_D^{Ge} from less than one to greater than one is responsible for the reversal of slope. The experiments also showed that K_D^{Ni} was insensitive to the P levels and was equal to 0.87. The positive slope on the log Ge vs log Ni is therefore associated with $K_D^{Ge} < 1$ and a negative slope with $K_D^{Ge} > 1$. The bulk P level determines K_D^{Ge} during successive stages of solidification and hence controls the shape of the curve on a log Ge vs log Ni plot. Group IVA meteorites have very low P levels and therefore the effect of P on K_D^{Ge} is negligible.

High P concentrations in the bulk alloy can lead to K_D^{Ge} being greater than unity very early in the solidification process. This will result in a negative slope on a log Ge vs log Ni plot. Groups I, IIAB and IIICD exhibit a negative slope as seen in Figure 1. These three groups have appreciable P levels in addition

to some S. It was pointed out earlier in Section E of the Results that S has a similar effect on the partitioning behaviour of Ge.

The positive slope of group IVA, the negative slope of groups I, IIAB and IIICD and the slope reversal in group IIIAB can be explained by the effect of P on K_D^{Ge}. An attempt was made to fit the simulated shapes on the log Ge vs log Ni plot to the actual shapes of meteorite chemical groups. The process was one of trial and error. Different bulk P, Ni, and Ge compositions were tried and the one yielding the best fit was chosen. The Ge and Ni contents determine the position of the curve on the log Ge vs log Ni plot while the P content dictates the shape of the curve. Good fits were obtained for groups IVA and IIIAB. Table 20 gives the bulk compositions that approximate the shapes of group IIIAB and group IVA. Figure 35 shows the actual chemical groups superimposed on the simulated curves. The '+' sign denotes the starting bulk composition. A quantitative study of the effect of S on K_D^{Ge} is required before a good fit can be expected for groups I, IIAB and IIICD.

Germanium contents in meteorites range from < 1 ppm to a few hundred ppm. The alloys used for studying the effect of P on K_D^{Ge} had between 0.5% and 1.0% Ge. The substantially higher Ge levels were required in the experimental alloys so that reliable and reproducible quantitative microprobe data could be obtained. As discussed earlier in this section Ge contents of up to 1 wt% did not have any noticeable effect on the liquidus and solidus line.

Group	Ni wt%	Ge (ppm)	P wt%
IIIAB	8.25	38.0	0.75
IVA	8.4	0.12	0.05

Table 20 - Simulated bulk compositions of groups IIIAB and IVA.

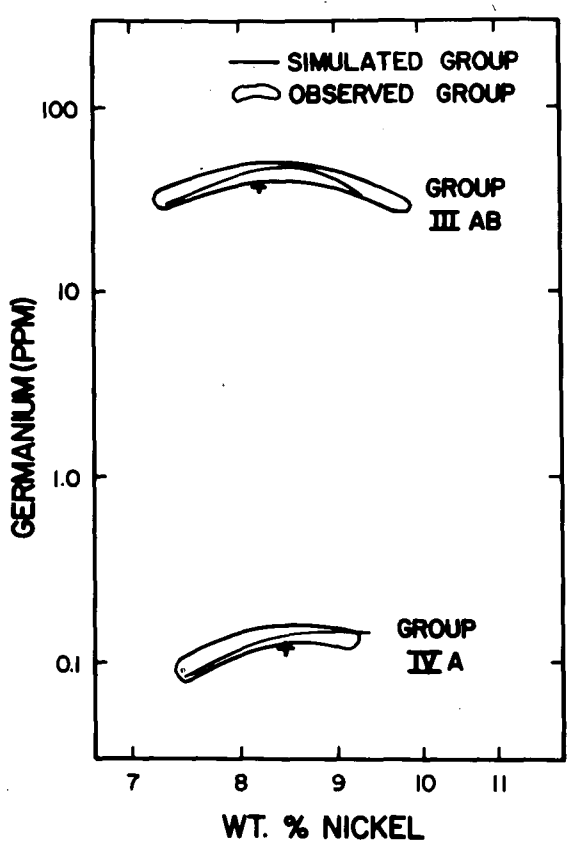

Fig. 35 - Matching the simulated shapes with the observed shapes of groups IIIAB and IVA.

Since P is the element that influences the solidus and liquidus compositions drastically, its effect on K_D^{Ge} can be assumed independent of the bulk Ge content provided the Ge level is < 1%. Therefore the observed effect of P on K_D^{Ge} can be extended to meteoritic Ge levels.

B.6. Implications of this work on cooling rate studies

The cooling rates experienced by meteorites can give valuable information about meteoritic parent bodies. Scott,[24] in his review paper, has mentioned that cooling rates in meteorites range from 0.3 to 1000°K/M yr. Cooling rates for groups IIC, IIIF, IVA, and IVB are in the range 10-500°K/M yr. while those for other groups and subgroups are in the range 1-10°K/M yr. The range of cooling rates within a group provides information about the distribution of the group members in their parent body. In the same review paper Scott has indicated that because metals have high thermal conductivities, meteorites from a single core should have similar cooling rates. It has been observed that many groups do have uniform cooling rates. Goldstein and Short[12] found that groups I and IIIB had uniform cooling rates. Randich and Goldstein[17] used metallographic techniques and concluded that groups IIA meteorites had reasonably uniform cooling rates. These observations are in agreement with the core-model for meteorite parent bodies. Similar cooling rate studies have also revealed that groups IIIA and IVA have cooling rates varying by over an order of magnitude.[17,36] Because groups IIIA and IVA are

both densely populated, the range of cooling rates observed within a group must be given some importance.

A variety of cooling rates observed in a group seems to contradict the core model for parent bodies. However, all cooling rate investigations are based on the width of the kamacite platelets in the Widmanstätten precipitate. Therefore the cooling rates deduced are valid only in the temperature range 300°C to 700°C where kamacite precipitates in a taenite matrix. The core model on the other hand, refers to the solidification of a molten Fe-Ni core and takes place in the temperature range 1500°C to 1000°C. The parent body after solidification and cooling to 1000°C can experience a fragmentation process. The different pieces get trapped in a larger parent body at different depths from the surface. Such an incorporation of smaller bodies in a bigger body has been discussed in Scott's review paper. The exact break up and incorporation sequence is, however, unclear. The pieces buried at different depths see different cooling rates when the temperature drops to the Widmanstätten precipitation range. Such a solidification, fragmentation, incorporation and cooling sequence is in line with the core model and also allows for meteorites in a group to have different cooling rates. The correlation between cooling rates and Ni contents that has been noticed in a few cases[36] cannot be explained at this stage.

B.7. The experimentally determined partition coefficients (K_D^X)

Precise quantitative modeling of the chemical fractionation observed in iron meteorite groups requires the knowledge of the equilibrium partition coefficients of the trace elements in iron-nickel alloys. Section C.2 of the background discusses some of the earlier attempts to experimentally determine the partition coefficients. Table 1 lists the K_D^X values published by different research groups. The different sets of data do not agree. The values reported by Goldstein and Friel[30] are, in comparison to other sets of data, closer to unity. This could be due to inadequate mixing in the liquid and or due to significant solid state diffusion during the experiments. It is interesting to note that their values agree well with the K_D^X values measured in this study. This implies that solid state diffusion did modify the K_D^X values measured by Goldstein and Friel (see Tables 1 and 9). The values reported by Bild and Drake[31] are on the other hand very different from unity. No explanation can be offered at this stage. Bild and Drake do not advocate the use of their K_D^X values in quantitative modeling. The equilibrium partition coefficients determined experimentally in this study agree well with the K_D^X values calculated by Scott[16] from the meteorite composition data. The close agreement in K_D^X values, as seen in Table 1, lends support to the cellular solidification model and the solid state diffusion effects proposed and described in this thesis.

SUMMARY

Experimental techniques and computer modeling were used to understand the trace element trends in Fe-Ni meteorites. The current Scott-Wasson theory predicts that plane front solidification is responsible for fractionation within a group. However plane front and cellular growth experiments accomplished in the laboratory together with thermal modeling of parent bodies indicate that these parent bodies would solidify dendritically rather than with a plane front. Fe-Ni-X alloys, where X is a third element, were solidified dendritically and the composition data from the dendrite cores and the bulk alloy were used to calculate the partition coefficients K_D^X of the ternary elements. These measured K_D^X values were corrected for solid state diffusion effects. A modification of the plate model developed by Flemings et al. (1970) was used for the correction. The diffusion calculations were done with a Crank Nicolson finite difference technique. A modified Gaussian elimination technique was used to solve the tri-diagonal matrix. The corrected equilibrium partition coefficients are: 0.43 for Au, 0.58 for Ge, 0.12 for P, 0.87 for Ni, 1.45 for Pt and 1.73 for Ir.

The major diffusion coefficients of Au and Ge, in Fe-Ni alloys, as a function of temperature were measured and used as inputs to the model. Further experimentation indicated that K_D^X values can be influenced significantly by elements that depress the melting point of Fe-Ni alloys. Group IIIAB meteorites have in-

creasing levels of P, an element that lowers the melting point of Fe-Ni alloys. In addition Ge-Ni correlations in group IIIAB show peculiar trends. Therefore the effect of P on K_D^{Ge} was investigated. The results show K_D^{Ge} increasing sharply from 0.58 to more than one for just 0.5% P in the solid. This functional dependence was incorporated into the segregation model. Changing the bulk P content in the model simulated the shapes of groups IVA and IIIAB. By adjusting the Ge and Ni bulk compositions, the simulated groups could be matched with the observed chemical groups. Preliminary experiments with S indicate that $K_D^{Ge} \gg 1$. This can be used to explain the negative slopes of groups I, IIAB and IIICD. A quantitative study of the effect of S on the partitioning of Ge will be necessary to simulate the correct shape of groups I, IIAB and IIICD.

REFERENCES

1. Moren, A. E.: Ph.D. Dissertation, Lehigh University, Bethlehem, PA, 1978.
2. Sears, D. W.: The nature and origin of meteorites. Monograph on Astronomical Subjects, Oxford University Press, New York, 1978.
3. Goldberg, E., Uchiyama, A. and Brown, H.: The distribution of nickel, cobalt, gallium, palladium and gold in iron meteorites. Geochim. Cosmochim. Acta. 2, pp. 1-25, 1951.
4. Lovering, J. F., Nichiporuk, W., Chodos, A. and Brown, H.: The distribution of gallium, germanium, cobalt, chromium and copper in iron and stony-iron meteorites in relation to nickel content and structure. Geochim. Cosmochim. Acta, 11, pp. 263-278, 1957.
5. Wasson, J. T.: The chemical classification of iron meteorites--I. A study of iron meteorites with low concentrations of gallium and germanium. Geochim. Cosmochim. Acta, 31, pp. 161-180, 1967.
6. Wasson, J. T. and Kimberlin, J.: The chemical classification of iron meteorites--II. Irons and pallasites with germanium concentrations between 8 and 100 ppm. Geochim. Cosmochim. Acta, 31, pp. 2065-2093, 1967.
7. Wasson, J. T.: The chemical classification of iron meteorites--III. Hexahedrites and other irons with germanium concentrations between 80 and 200 ppm. Geochim. Cosmochim. Acta, 33, pp. 859-876, 1969.

8. Wasson, J. T.: The chemical classification of iron meteorites--IV. Irons with germanium concentrations greater than 190 ppm and other meteorites associated with Group I. Icarus, 12, pp. 407-423, 1970a.

9. Wasson, J. T. and Schaudy, R.: The chemical classification of iron meteorites--V, Groups IIIC and IIID and other irons with germanium concentrations between 1 and 25 ppm. Icarus, 14, pp. 59-70, 1971.

10. Scott, E. R. D. and Wasson, J. T.: Classification and properties of iron meteorites. Rev. Geophys. and Space Physics, 13, 4, pp. 527-546, 1975.

11. Wood, J. A.: The cooling rates of parent planets of several iron meteorites. Icarus, 3, pp. 429-459, 1964.

12. Goldstein, J. I. and Short, J. M.: Cooling rates of 27 iron and stony-iron meteorites. Geochim. Cosmochim. Acta, 31, pp. 1001-1023, 1967a.

13. Goldstein, J. I. and Short, J. M.: The iron meteorites. Their thermal history and parent bodies, Geochim. Cosmochim. Acta, 31, pp. 1733-1770, 1967b.

14. Reed, S. J. B.: Electron probe microanalysis of the metallic phases in meteorites. Geochim. Cosmochim. Acta, 29, pp. 535-549, 1965.

15. Goldstein, J. I. and Ogilvie, R. E.: The growth of Widmanstätten pattern in metallic meteorites. Geochim. Cosmochim. Acta, 29, pp. 893-920, 1965.

16. Scott, E. R. D.: Chemical fractionation in iron meteorites and its interpretation. Geochim. Cosmochim. Acta, 36, pp. 1205-1236, 1972.

17. Goldstein, J. I. and Randich, E.: Cooling rates of hexahedrites. Geochim. Cosmochim. Acta, 42, pp. 141-150, 1978.

18. Wasson, J. T. and Wetherill, G. W.: Physical and chemical processes involved in the formation of the iron meteorites. Unpublished manuscript. NAPS Document 01742.

19. Anders, E.: Origin, age and composition of meteorites. Space Sci. Rev., 3, pp. 583-714, 1964.

20. Kelly, R. W. and Larimer, J. W.: Chemical fractionation in meteorites--VIII. Iron meteorites and the cosmochemical history of the metal phase. Geochim. Cosmochim. Acta, 41, pp. 93-111, 1977.

21. Sears, D. W.: Condensation and the composition of iron meteorites. Earth Planet. Sci. Letters, 41, pp. 128-138, 1978a.

22. Sears, D. W.: Did iron meteorites form in the asteroid belt? Evidence from thermodynamic models. Icarus (special asteroid issue), 1979.

23. Wasson, J. T. and Wai, C. M.: Explanations for the low Ga and Ge concentrations in some iron meteorites. Nature, 261, pp. 114-116, 1976.

24. Scott, E. R. D.: Origin of iron meteorites, Asteroids, ed. Gehrels, T. and Matthews, M. S., pp. 892-925, 1979.

25. Wetherill, G. W.: Collisions in asteroid belt. J. Geophys. Res., 72, pp. 2429-2444, 1967.

26. Scheil, E.: Z. Metallk., 34:70, 1942.

27. Chalmers, B.: Principles of Solidification. John Wiley & Sons Inc., New York, p. 140, 1964.

28. Flemings, M. C.: Solidification processing. McGraw Hill, New York, p. 87, 1974.

29. Coates, D. E., Subramanian, S. V. and Purdy, G. R.,: Solid-liquid interface stability during solidification of dilute ternary alloys, Trans. AIME, 242, p. 800, 1968.

30. Goldstein, J. I. and Friel, J. J.: Fractional crystallisation of a liquid iron core, an experimental study. Proc. Lunar Planet. Sci. Conf. 9th, pp. 1423-1435, 1978.

31. Bild, R. W. and Drake, M. J.: Experimental investigation of trace element fractionation in iron meteorites: I Early results. Proc. Lunar Planet. Sci. Conf. 9th, pp. 1407-1421, 1978.

32. Rutter, J. W. and Chalmers, B.: A prismatic substructure formed during solidification of metals. Can. J. of Phys. 31, p. 15, 1953.

33. Hucke, E., Adams, C., Flemings, M. C. and Taylor, H. F.: Physical Chemistry of Process Metallurgy--Part II, p. 815, Interscience Publishers, Inc. New York, 1961.

34. Brody, H. D. and Flemings, M. C.: Solute redistribution in dendritic solidification. Trans. AIME, 236, pp. 615-624, 1966.

35. Flemings, M. C., Poirier, D. R., Barone, R. V. and Brody, H. D.: Microsegregation in iron-base alloys. J. Iron and Steel Inst., 208, pp. 371-381, 1970.

36. Goldstein, J. I. and Moren, A. E.: Cooling rates of group IVA iron meteorites from a ternary Fe-Ni-P model. Earth and Planetary Sci. Letters, 43, pp. 182-196, 1979.

37. Romig, A. D., Jr.: M.S. Thesis, Lehigh University, Bethlehem, PA, 1977.

38. Practical Scanning Electron Microscopy: ed. Goldstein, J. I. and Yakowitz, H., Plenum Press, New York p. 582, 1975.

39. Reed-Hill, R. E.: Physical Metallurgy Principles. D. Van Nostrand Company, New York, p.920, 1973.

40. Hellawell, A. and Hume-Rothery, W.: Phil. Trans. Royal Society of London, 249A, pp. 417-459, 1957.

41. Houghton, J. L.: Alloys of Iron Research--Part VIII, J. Iron and Steel Inst., 115, pp. 417-433, 1927.

42. Doan, A. S., Jr. and Goldstein, J. I.: The ternary phase diagram, Fe-Ni-P. Met. Trans. 1, pp. 1759-1767, June 1970.

43. Von Rosenberg, D. U.: Modern analytic and computational methods in science and mathematics. Am. Elsevier Publ. Co., New York, 1969.

44. Roache, P. J.: Computational fluid dynamics, Hermosa Publishers, Box 8172, Albuquerque, New Mexico, p. 345, 1972.

45. Onsager, L.: Ann. N.Y. Acad. Sci., 46, p. 241, 1945.

46. Kirkaldy, J. S.: Advan. Mater. Res., 4, p. 55, 1970.

47. Goldstein, J. I., Hanneman, R. E. and Ogilvie, R. E.: Diffusion in the Fe-Ni system at 1 atm. and 40 Kbar pressure. Trans. TMS-AIME, 233, pp. 812-820, 1965.

48. Heyward, T. R. and Goldstein, J. I.: Ternary diffusion in the α and γ phases of the Fe-Ni-P system. Met. Trans., 4, pp. 2335-2342, 1973.

49. Kucera, J. and Million, B.: Diffusion of Pt in Fe-Pt alloys. Physica Status solidi (a), 31(1), pp. 275-282, 1975.

50. Froschhammer, D., Tensi, H. M., Zoller, H. and Feurer, U.: Diffusion in the liquid near the moving solid-liquid interface of an Al-0.3% Cu alloy. Met. Trans. (B), 11B, p. 169, March 1980.

51. Goldstein, J. I., Narayan, C. and Soroka, W. : unpublished work.

52. Barone, R. V., Brody, H. D. and Flemings, M. C.: Investigation of solidification of high strength steel castings, interim report. Tech. report number AMRA CR64-0413, Dept. of Army Project No. 1A02440A110.

53. Fricker, P. E., Goldstein, J. I. and Summers, A. L.: Cooling rates and thermal histories of irons and stony-iron meteorites. Geochim. Cosmochim. Acta, 34, pp. 475-491, 1970.

54. Buchwald, V. F.: Handbook of Iron Meteorites, No. 1, Univ. of California Press, 1975.

APPENDIX I

```
RFL(25000)
RUNT.
MAP(PART)
LGO.
      PROGRAM COMPO(INPUT,OUTPUT,TAPE5=INPUT,TAPE6=OUTPUT)
      REAL LENGTH,LAMDA,KELEM,LENGTHM,KPNI,KPEL,KNICKEL
      REAL KPHOS
      DIMENSION CNI(125),CONI(125),CEL(125),COEL(125),X(125)
      DIMENSION ENI(125),FNI(125),EEL(125),FEL(125)
      READ(5,101) CONI,COEL,LENGTH,KELEM
101   FORMAT(4E10.2)
      READ(5,789) OZERO,Q
C           CONI IS THE BULK NI CONTENT.
C           COEL IS THE BULK CONTENT OF THE THIRD ELEMENT X
C           LENGTH IS THE SEMI DENDRITE WIDTH
C           KELEM IS THE ASSUMED EQLB PARTITION COEF. OF X
C           Q IS THE ACTIVATION ENERGY FOR X (CAL.)
C           OZERO IS THE FREQUENCY FACTOR FOR ELEMENT X
789   FORMAT(2E10.2)
      TEMP=1773.0
C           K FOR NI IS ASSUMED AS 0.87
      KNICKEL=0.87
      SIGMAN=0.0
      SIGMAE=0.0
      LAMDA=0.00
      DELX=(LENGTH-0.05E-04)/100.0
      CLION=CONI
      CLIOE=COEL
      X(1)=-DELX*1.0E04
      DO 12 I=2,102
12    X(I)=X(I-1)+(DELX*1.0E04)
C*****  CALCULATION OF THE INITIAL SEGREGATION PROFILE FOR NI AND **.
C           K FOR P IS ASSUMED AS 0.2
      KPHOS=0.2
C           ADJUSTING THE BULK P CONTENT
      CZERO=0.05
      CPHOS=CZERO*KPHOS

C*****DETERMINING THE SOLIDIFICATION RANGE
      SRANGE=CZERO*100.0/0.25
      IF(CZERO.GT.1.25) SRANGE=500.0
C*****CALCULATING DELTA TIME BASED ON THIS RANGE
      DELT=SRANGE/100.0


      DO 22 J=2,101
      CNI(J)=CLION*KNICKEL
C*****************  K GERMANIUM VARIES AS A FUNCTION OF PHOS CONTENT.
      KELEM=CPHOS*1.06+0.54
      CEL(J)=CLIOE*KELEM
      LAMDA=LAMDA+DELX
      SIGMAN=SIGMAN+CNI(J)
      SIGMAE=SIGMAE+CEL(J)
      FSOLID=LAMDA/LENGTH
      CPHOS=KPHOS*CZERO*((1.0-FSOLID)**(KPHOS-1.0))
      OUTPUT,KELEM,CPHOS
      CLION=(CONI-DELX*SIGMAN/LENGTH)/(1.0-FSOLID)
      CLIOE=(COEL-DELX*SIGMAE/LENGTH)/(1.0-FSOLID)
      CONI(J)=CNI(J)
      COEL(J)=CEL(J)


C*****  CALCULATING THE EFFECT OF DIFFUSION ON THE SEGREGATION PROFILE.
C*****  THE CRANK-NICHOLSON TECHNIQUE IS USED TO SET UP THE TRI-DIAGONAL MATRIX.
C*****  ROACHE ALGORITHM IS EMPLOYED TO SOLVE THE TRI-DIAGONAL MATRIX.
      IF(J.LT.5.0) GO TO 22
C*****  INTRODUCING THE DIFFUSIVITY DATA.
      A=EXP(1.15+0.0519*CONI)
      B=EXP(-(76400.0-11.6*CONI)/(1.987*TEMP))
      DNI=A*B

      DEL=OZERO*EXP(-Q/(1.987*TEMP))
```

```
      CONI(1)=CONI(3)
      CDEL(1)=CDEL(3)
      CONI(J+1)=CONI(J-1)
      CDEL(J+1)=CDEL(J-1)
      OUTPUT.A,B,ONI,DEL,A88NI,A88EL
      A88NI=2.0*((DELX**2.0)/(DNI*DELT))
      A88EL=2.0*((DELX**2.0)/(DEL*DELT))
      B8NI=2.0+A88NI
      B8EL=2.0+A88EL
      BONI=-2.0+A88NI
      BOEL=-2.0+A88EL
      ENI(2)=1.0
      EEL(2)=1.0
      FNI(2)=0.0
      FEL(2)=0.0
      MM=J-1
      DO 62 M=3,MM
      DENI=B8NI-ENI(M-1)
      DEEL=B8EL-EEL(M-1)
      ENI(M)=1.0/DENI
      EEL(M)=1.0/DEEL
      ADNI=CONI(M-1)+BONI*CONI(M)+CONI(M+1)
      ADEL=CDEL(M-1)+BOEL*CDEL(M)+CDEL(M+1)
      FNI(M)=(ADNI+FNI(M-1))/DENI
62    FEL(M)=(ADEL+FEL(M-1))/DEEL
      CONI(J)=FNI(MM)/(1.0-ENI(MM))
      CDEL(J)=FEL(MM)/(1.0-EEL(MM))
      DO 72 MK=2,MM
      M=J+1-MK
      CONI(M)=ENI(M)*CONI(M+1)+FNI(M)
72    CDEL(M)=EEL(M)*CDEL(M+1)+FEL(M)
      TEMP=TEMP-DELT


      OUTPUT,FSOLID,CEL(J),SIGMAE
22    CONTINUE
      DELT=0.25
C***** CALCULATING THE EFFECT OF DIFFUSION ON THE SEGREGATION PROFILE.
C***** THE CRANK-NICHOLSON TECHNIQUE IS USED TO SET UP THE TRI-DIAGONAL MATRIX.
C***** ROACHE ALGORITHM IS EMPLOYED TO SOLVE THE TRI-DIAGONAL MATRIX.
      IJK=(TEMP-1223.0)/0.25
C*****DETERMINES NUMBER OF ITERATIONS REQUIRED IN THE ALL SOLID STATE
      DO 32 J=1,IJK
C***** INTRODUCING THE DIFFUSIVITY DATA.
      A=EXP(1.15+0.0519*CONI)
      B=EXP(-(76400.0-11.6*CONI)/(1.987*TEMP))
      DNI=A*B

      DEL=DZERO*EXP(-Q/(1.987*TEMP))

      CONI(1)=CONI(3)
      CDEL(1)=CDEL(3)
      CONI(102)=CONI(100)
      CDEL(102)=CDEL(100)
      A88NI=2.0*((DELX**2.0)/(DNI*DELT))
      A88EL=2.0*((DELX**2.0)/(DEL*DELT))
      B8NI=2.0+A88NI
      B8EL=2.0+A88EL
      BONI=-2.0+A88NI
      BOEL=-2.0+A88EL
      ENI(2)=1.0
      EEL(2)=1.0
      FNI(2)=0.0
      FEL(2)=0.0
      MM=101-1
      DO 42 M=3,MM
      DENI=B8NI-ENI(M-1)
      DEEL=B8EL-EEL(M-1)
      ENI(M)=1.0/DENI
      EEL(M)=1.0/DEEL
      ADNI=CONI(M-1)+BONI*CONI(M)+CONI(M+1)
      ADEL=CDEL(M-1)+BOEL*CDEL(M)+CDEL(M+1)
      FNI(M)=(ADNI+FNI(M-1))/DENI
42    FEL(M)=(ADEL+FEL(M-1))/DEEL
      CONI(101)=FNI(MM)/(1.0-ENI(MM))
      CDEL(101)=FEL(MM)/(1.0-EEL(MM))
      DO 52 MK=2,MM
      M=102-MK
      CONI(M)=ENI(M)*CONI(M+1)+FNI(M)
52    CDEL(M)=EEL(M)*CDEL(M+1)+FEL(M)
      TEMP=TEMP-DELT
32    CONTINUE
```

```
      LENGTHM=LENGTH*1.0E04
      TEMPC=TEMP-273.0
      KFNI=CONI(2)/CONI
      KFEL=CDEL(2)/COEL
      WRITE(6,200) CONI,COEL
200   FORMAT(//,5X,*INITIAL HOMOGENEOUS COMPOSITION OF THE VOLUME ELEMEN
     1T IS *,F5.2,* WT. PERCENT NICKEL AND *,E10.2,* WT. PERCENT OF TERN
     1ARY ELEMENT.*)
      WRITE(6,201) KNICKEL,KELEM
201   FORMAT(//,5X,*THE ASSUMED PARTITION COEFFECIENTS ARE  *,F4.2,* FOR
     1NICKEL AND  *,F4.2,*  FOR THE THIRD ELEMENT.*)
      WRITE(6,202) LENGTHM
202   FORMAT(//,5X,*THE DISTANCE FROM CELL CENTRE TO EDGE IS *,F6.2,* MI
     1CRONS*)
      WRITE(6,203)
203   FORMAT(//,5X,*SOLIDIFICATION STARTS AT 1500 DEG CELSIUS AND THE TE
     1MPERATURE DROP IS 1 DEG PER SECOND.*)
      WRITE(6,204)
204   FORMAT(////,5X,*DISTANCE FROM CELL CENTRE*,3X,*NI WT PERCENT*,5X,*
     1NI WT. PERCENT*,5X,*-- WT. PERCENT*,5X,*-- WT. PERCENT*)
      WRITE(6,205)
205   FORMAT(13X,*(MICRONS)*,13X,*BEFORE DIFFUSION*,2X,*AFTER DIFFUSION-
     1,2X,*BEFORE DIFFUSION*,2X,*AFTER DIFFUSION*)
      OUTPUT,TEMP
      DO 82 K=2,101
      WRITE(6,206) X(K),CNI(K),CDNI(K),CEL(K),CDEL(K)
206   FORMAT(16X,F5.2,17X,E10.2,10X,E10.2,10X,E10.2,10X,E10.2)
82    CONTINUE
      WRITE(6,207)
207   FORMAT(//,5X,*THE TEMP HAS FALLEN TO 1000DEG CELSIUS AND DIFFUSION
     1 HEREAFTER IS IGNORED*)
      WRITE(6,208) KFNI,KFEL
208   FORMAT(//,5X,*THE PARTITION COEFS. SEEN IN THE FINAL PROFILE ARE *
     1,F5.2,* FOR NICKEL AND  *,F5.2,* FOR THE THIRD ELEMENT.*)
      CEL(1)=CEL(3)
      CNI(1)=CNI(3)
      CDNI(1)=CDNI(3)
      CDEL(1)=CDEL(3)
      DELTAN=0.07
      DELTAE=0.5
      FNI=6.0
      IF(CDEL(2).GT.CDEL(101)) FEL=CEL(99)/1.5
      IF(CDEL(2).LT.CDEL(101)) FEL=  CEL(2)/1.5
      FEL=4.0E-06
C***** THE CONCENTRATION OF THE THIRD ELEMENT IS PLOTTED AS A FUNCTION
C*****  OF THE CONCENTRATION OF NICKEL ON A LOG-LOG PLOT.
C*****  EACH POINT ON THIS PLOT NOW REPRESENTS A METEORITE BECAUSE  THE
C*****  COMPOSITIONS  OF THE TWO ELEMENTS COME FROM THE SAME POINT ON
C*****  THE DENDRITE.
C******THIS REDEFINITION OF CONCENTRATIONS IS FOR PLOTTING ONLY.THIS
C******NOW CONFORMS TO THE *LGLINE* PLOTTER FORMAT.
      CDNI(98)=FNI
      CDNI(99)=DELTAN
      CDEL(98)=FEL
      CDEL(99)=DELTAE
      CNI(98)=FNI
      CNI(99)=DELTAN
      CEL(98)=FEL
      CEL(99)=DELTAE

      CALL LGAXIS(1.0,1.0,18H NICKEL WT PERCENT,-18,6.0,0.0,FNI,DELTAN)
      CALL LGAXIS(1.0,1.0,15H WT. PERCENT GE,15,8.0,90.0,FEL,DELTAE)
      CALL LGAXIS(1.0,9.0,18H NICKEL WT PERCENT,18,6.0,0.0,FNI,DELTAN)
      CALL LGAXIS(7.0,1.0,15H WT. PERCENT GE,-15,8.0,90.0,FEL,DELTAE)
      CALL PLOT(1.0,1.0,-3)
      CALL LGLINE(CNI,CEL,97,1,-5,1,0)
      CALL LGLINE(CDNI,CDEL,97,1,-5,11,0)
      STOP
      END
8.35          0.09E-04 50.05E-040.58
  0.492   61856.0
```

VITA

C. Narayan was born to Mr. and Mrs. C. N. Chandrasekhar on April Fool's Day in the year 1956 in Madras, India. He attended a variety of schools in numerous cities and finished high school in 1973. He then joined the Indian Institute of Technology at Madras, India where he started his career as a metallurgist. Having graduated with a bachelor's degree in metallurgy he came to Lehigh for graduate school in 1978 where he is currently working on a doctoral program.